



REGENERATION

Rehabilitation exercise-driven symbiotic electrical stimulation system accelerating bone regeneration

Tianlong Wang^{1,2†}, Han Ouyang^{3†}, Yiping Luo^{1,2†}, Jiangtao Xue⁴, Engui Wang³, Lei Zhang^{1,2}, Zifei Zhou^{1,2}, Zhiqing Liu^{1,2}, Xifan Li¹, Shuo Tan¹, Yixing Chen^{1,2}, Liping Nan¹, Wentao Cao^{1,5*}, Zhou Li^{3,4*}, Feng Chen^{1,5*}, Longpo Zheng^{1,2*}

Electrical stimulation can effectively accelerate bone healing. However, the substantial size and weight of electrical stimulation devices result in reduced patient benefits and compliance. It remains a challenge to establish a flexible and lightweight implantable microelectronic stimulator for bone regeneration. Here, we use self-powered technology to develop an electric pulse stimulator without circuits and batteries, which removes the problems of weight, volume, and necessary rigid packaging. The fully implantable bone defect electrical stimulation (BD-ES) system combines a hybrid tribo/piezoelectric nanogenerator to provide biphasic electric pulses in response to rehabilitation exercise with a conductive bioactive hydrogel. BD-ES can enhance multiple osteogenesis-related biological processes, including calcium ion import and osteogenic differentiation. In a rat model of critical-sized femoral defects, the bone defect was reversed by electrical stimulation therapy with BD-ES and subsequent bone mineralization, and the femur completely healed within 6 weeks. This work is expected to advance the development of symbiotic electrical stimulation therapy devices without batteries and circuits.

INTRODUCTION

Bone defects (BDs), which are caused by trauma, osteitis, or bone tumors, represent a serious problem in public health. Postoperative rehabilitation problems include prolonged hospitalization, postsurgery complications, and increased treatment costs, placing a considerable burden on patients. Clinical intervention via direct graft using autologous or allograft bone for repairing the critical-sized defects is relatively successful, but these therapeutics are generally limited by difficulties in sourcing bones, contour adaptation, and immunological rejection (1, 2). Recently, mimicking the osteogenic microenvironment using implanted synthetic scaffolds has emerged as a promising strategy to regulate the extracellular microenvironment at the wound site to accelerate bone regeneration (3, 4). However, it is still insufficient to rely solely on pure biomaterials for BD repair in vivo due to the inefficiency of bone regeneration after implantation. Moreover, the indispensable role of physical cues such as bioelectricity in the bone microenvironment is often ignored, and it has been reported that mechanical stimuli can be converted into electrical signals by altering the activities of mechanosensitive channels represented by the Piezo family (5, 6). However, the BD area often lacks an endogenous electric field because it cannot sense mechanical stimuli, leading to disruption of the microenvironment (7).

Electrical stimulation (ES), as an important biophysical level regulator and a nonpharmacological intervention in clinical practice,

has received considerable attention because of its remarkable ability to modulate cell activity and enhance tissue repair (8–10). However, the detailed mechanisms of ES in promoting bone repair are poorly understood, and the widespread use of current ES therapies is limited by bulky external equipment and complex operation management. Most recently, researchers found that biofeedback ES therapy, which enables the correlation of stimulation parameters to dynamic locomotion, displays a more notable therapeutic effect than conventional ES for musculoskeletal injury (11). As a promising candidate for future energy technology, emerging nanogenerators (NGs) can transform mechanical energy into electricity based on the triboelectric or piezoelectric effect (12–15). Since their invention, numerous NGs have been reported in various applications, such as self-powered sensing (16–19), smart agriculture (20), blue energy harvesting (21), electrocatalysis (22), and other fields (23–26). In particular, NGs can synchronously convert human body motions into pulsed electrical signals and thus have great potential for application in self-powered and self-responsive ES therapy (27–31). Our recent work revealed that NGs with pulsed electrical signals can promote osteoblast attachment, proliferation, and differentiation, which are mainly attributed to the up-regulation of intracellular Ca^{2+} levels (32). However, despite the proven positive effect in vitro, there are only a few reports on NGs for orthopedic trauma repair to date.

Hence, we propose a self-powered, fully implantable BD-ES system that consists of an unusual flexible hybrid tribo/piezoelectric nanogenerator (HTP-NG) and a conductive injectable hydrogel to construct an osteogenic microenvironment of the defect region by inducing multiple biological processes (Fig. 1A) (33). The designed HTP-NG device was implanted into the subcutaneous tissue of the thigh to produce biphasic electric pulses driven by knee joint movements, which were then conducted into the BD area for ES therapy (Fig. 1, B and C). Meanwhile, inspired by the physiological biomineralization process, a conductive hydrogel with multiple functions was constructed by the addition of polydopamine-modified black phosphorus nanosheets (BP@PDA) and alginate methacryloyl (AlgMA) to an extracellular

¹Center for Orthopaedic Science and Translational Medicine, Department of Orthopedics, Shanghai Tenth People's Hospital, School of Medicine, Tongji University, Shanghai 200072, China. ²Orthopedic Intelligent Minimally Invasive Diagnosis and Treatment Center, Shanghai Tenth People's Hospital, School of Medicine, Tongji University, Shanghai 200072, China. ³School of Nanoscience and Engineering, University of Chinese Academy of Sciences, Beijing 100049, China. ⁴Beijing Key Laboratory of Micro-Nano Energy and Sensor, Beijing Institute of Nanoenergy and Nanosystems, Chinese Academy of Sciences, Beijing 101400, China. ⁵Shanghai Key Laboratory of Craniomaxillofacial Development and Diseases, Stomatological Hospital and School of Stomatology, Fudan University, Shanghai 201102, China. *Corresponding author. Email: wt_cao@fudan.edu.cn (W.C.); zli@binn.cas.cn (Z. Li); fchen@tongji.edu.cn (F.C.); dr.zheng@tongji.edu.cn (L. Zheng) †These authors contributed equally to this work.

matrix (ECM) network for electroactive tissue repair. As a natural semiconductor with high electrical conductivity, BP enables efficient electron transport and can be degraded to PO_4^{3-} , which is one of the main components of bone tissue and can be used for mineralization (34). However, the intrinsic instability of BP limits its clinical application. As a biocompatible and biodegradable material, polydopamine (PDA) could modify the surface of BP, enhancing its water dispersion and stability. Furthermore, PDA modification leads to enhanced interfacial bonding between the unmodified BP nanosheets and the hydrogel matrix, and the integration of BP@PDA greatly improves the electrical conductivity of the hydrogel, which makes its application in the biomedical field possible (35).

In addition to promoting cell proliferation and enhancing cell migration, the BD-ES system facilitated osteogenic differentiation both in vitro and in vivo. Moreover, mRNA sequencing analysis revealed that the BD-ES system supported angiogenesis and skeletal system development and up-regulated the expression of osteogenesis-related proteins and several mechanosensitive proteins involved in the phosphatidylinositol 3-kinase (PI3K)/AKT, WNT, and mitogen-activated protein kinase (MAPK) signaling pathways, which play a positive role in osteogenesis (Fig. 1D). In particular, the BD-ES system has great potential to be applied in the clinic to promote bone repair because early functional exercise is necessary (36, 37), can effectively reduce local adhesions and edema formation, and improves joint flexibility and muscle strength. Patients with BDs are

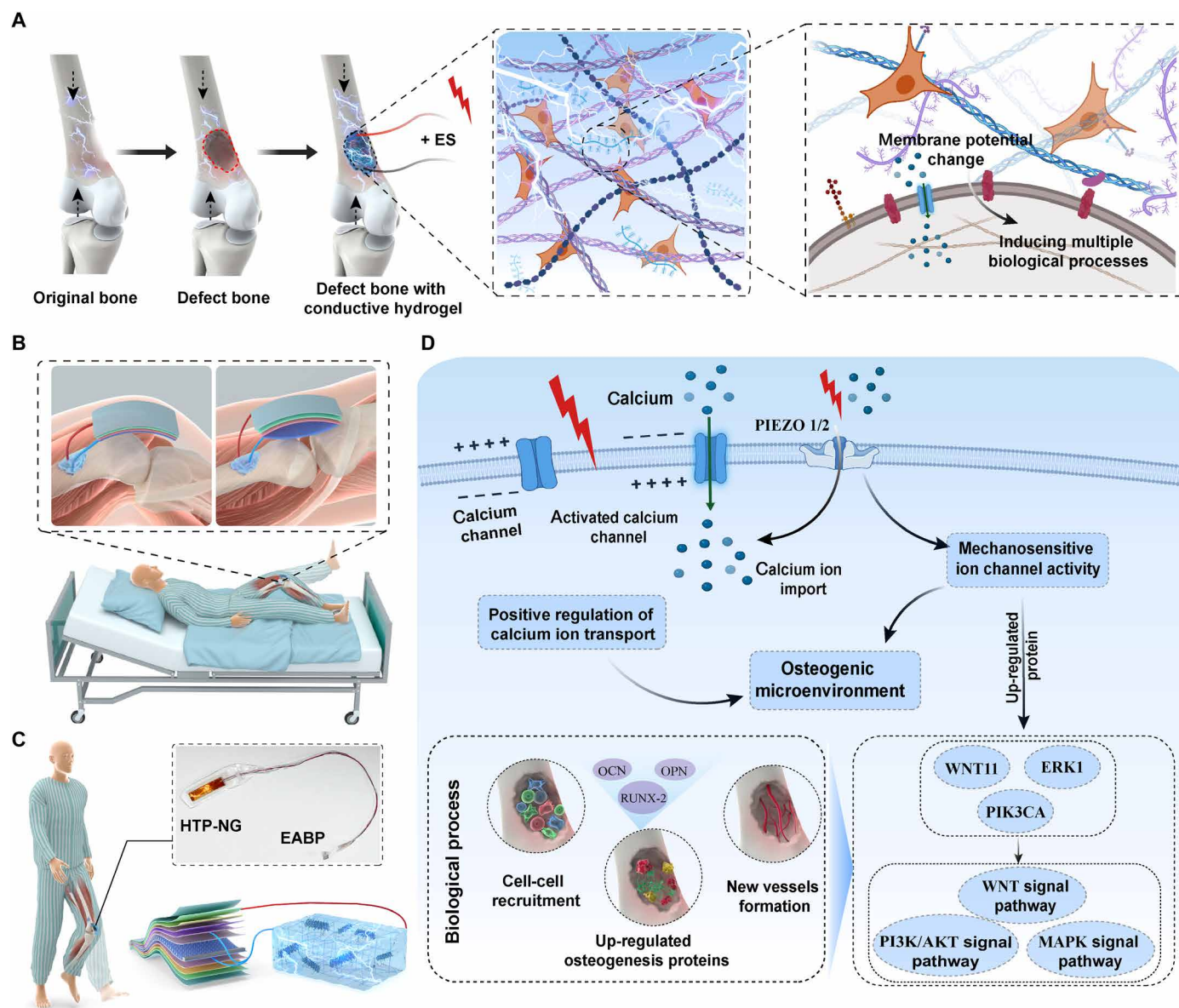


Fig. 1. Schematic of the main concept for a fully implantable BD-ES system. (A) Schematic of the reconstruction of the electrical microenvironment to accelerate bone regeneration in the bone defect region using ES. (B and C) Schematic of a fully implantable battery-free BD-ES system for patients performing active or passive functional exercise under guidance (D). Possible mechanism by which the BD-ES system promotes bone repair.

often asked to exercise on a bed or with weight-bearing, based on their condition, under guidance (38). As a result, exercise not only reduces postoperative complications but also shows great potential in bone repair via the generation of biphasic electric pulses driven by HTP-NG from joint movements, which provides an opportunity to restore the microenvironment at the defect site. Thus, the development of an implantable therapeutic system to promote bone regeneration and repair is highly urgent for future clinical applications and may be a promising pathway for accelerating the treatment of BDs. Overall, by integrating mechanical and electrical stimuli, this study provides new insight into personalized bone regeneration and demonstrates the potential mechanism by which the BD-ES system alters the microenvironment.

RESULTS

Design and integration of the fully implantable BD-ES system

To accelerate bone regeneration, a fully implantable battery-free BD-ES system was applied in vivo. The advanced BD-ES system consisted of two modules: (i) a power generation module based on an HTP-NG device and (ii) a bioactive conductive hydrogel based on cross-linked networks of ECM grafted with AlgMA and BP@PDA. In contrast to previous studies, which required an external power supply to provide ES for promoting bone repair (39, 40), we used a multilayer assembly strategy to design a hybrid NG (fig. S1) for producing stable electricity. The capacity of HTP-NG to convert mechanical energy into electricity enabled it to generate biofeedback biphasic electric pulses in response to knee joint movements. After implanting HTP-NG into thigh subcutaneous tissue, the BD site was filled with cross-linked ECM-AlgMA-BP@PDA (EABP) hydrogel. The bioactive EABP hydrogel and the charges produced by HTP-NG acted synergistically to enhance bone tissue regeneration.

Fabrication and characterization of HTP-NG

The implantable HTP-NG device was designed on the basis of a hybrid piezoelectric and triboelectric effect. The disassembled HTP-NG structure consisted of triboelectric, piezoelectric, and encapsulation modules (Fig. 2A and table S1). The core part of the HTP-NG was its triboelectric and piezoelectric modules, which were capable of capturing knee joint motion energy to produce electricity. The piezoelectric module was primarily composed of a commercial polarized polyvinylidene fluoride (PVDF) film and two silver (Ag) electrode layers. Because of the substantial difference in electronegativity between polytetrafluoroethylene (PTFE) and Ag, the PTFE and Ag layers served as a negatively and a positively charged dielectric material, respectively. To enhance the HTP-NG output performance, the corona discharge method was used to increase the effective contact area and surface charge density of the PTFE dielectric layer (fig. S2B). By ionizing and producing an area of plasma around the corona needle, which had a high potential, the current traveled from the needle into the atmosphere. After corona polarized treatment, a PTFE film with a nanostructured surface was obtained (fig. S2, C and D). To avoid liquid leakage and interference, the HTP-NG was eventually packaged in a dielectric Teflon film and a thin polydimethylsiloxane (PDMS) layer. Due to the optimized material selection and structural design, the HTP-NG device possessed exceptional flexibility and miniature dimensions, ensuring effective contact with subcutaneous soft tissues. To efficiently capture the biomechanical

energy produced by knee joint motions, an implantable HTP-NG device was constructed on the basis of the combination of piezoelectric and triboelectric effects. Last, the HTP-NG had an improved electromechanical conversion ability compared to a single triboelectric or piezoelectric module (fig. S3).

The working principle of the HTP-NG could be explained as the combined effect of the triboelectric and piezoelectric components (Fig. 2A). In the initial state, there was no triboelectric or piezoelectric potential between the various electrodes because the top layer was isolated from the bottom layer. When a force was applied to the HTP-NG, the PVDF film bent and generated a piezoelectric potential on its surface. Meanwhile, contact between the curved Ag layer and PTFE layer caused charge transfer between the two films due to the triboelectric effect. This charge transfer created a potential difference between the Al electrode on the PTFE film and the Ag layer. As the deformation of the PTFE film was maximized, the system established a new equilibrium, where the triboelectric and piezoelectric potentials both approached peak levels. Therefore, a current would appear during the HTP-NG deformation process if an external circuit was used to connect the electrodes. When the pressure was released, the curved PVDF film started to recover its original state, and thus, the electrons flowed back from the upper Ag electrode and Al layer to the bottom Ag electrode, which resulted in a reverse current in the external circuit. In addition, because of the complexity of the operating environment of the device, there may still be freestanding piezoelectric and triboelectric modes of the HTP-NG. Additional working principles and equivalent electrical circuit models of the HTP-NG in the freestanding piezoelectric and triboelectric modes are also displayed (fig. S4).

To investigate the in vitro electrical output performance of the HTP-NG, a modal shaker was used to simulate normal biomechanical movements at low frequencies. The open-circuit voltage (V_{OC}), short-circuit current (I_{SC}), and corresponding short-circuit transferred charge (Q_{SC}) of the HTP-NG were approximately 35 V, 3.7 μ A, and 23 nC, respectively (Fig. 2B and table S2). The electrical output strongly matched the input pressure waveform, demonstrating excellent cooperativity between the force and electricity of the HTP-NG (Fig. 2C and fig. S5). Moreover, V_{OC} of HTP-NG increased as the applied force rose, displaying a notable linear relationship with a slope of 5.33 (Fig. 2, D and E). The electrical output performance of the HTP-NG device was positively correlated with its working area (fig. S6, A to C). As the working area increased from 0.5 cm \times 2 cm to 2 cm \times 8 cm, V_{OC} of HTP-NG increased from 35 to 530 V (table S3). Considering the general advantages of the conformal dimension and output performance together, HTP-NG with a working area of 0.5 cm \times 2 cm was selected for further in vitro and animal studies. The HTP-NG device also displayed various output performances at a series of frequencies. V_{OC} of HTP-NG remained stable at different frequencies, while I_{SC} improved with increasing operating frequency (fig. S6, D to F), which could be attributed to the higher frequency leading to more rapid charge transfer. Meanwhile, the HTP-NG displayed remarkable stability and durability (approximately 5000 cycles of mechanical stimuli at constant frequency) and no fluctuations in power generation capability (Fig. 2F and fig. S7). Further evaluations of the effective electric power of the HTP-NG showed that the instantaneous voltage increased and the current decreased with increasing external resistance (fig. S8A). The largest instantaneous power density of approximately 344.4 mW m⁻² was achieved at an external load of 30 megohms, which enabled

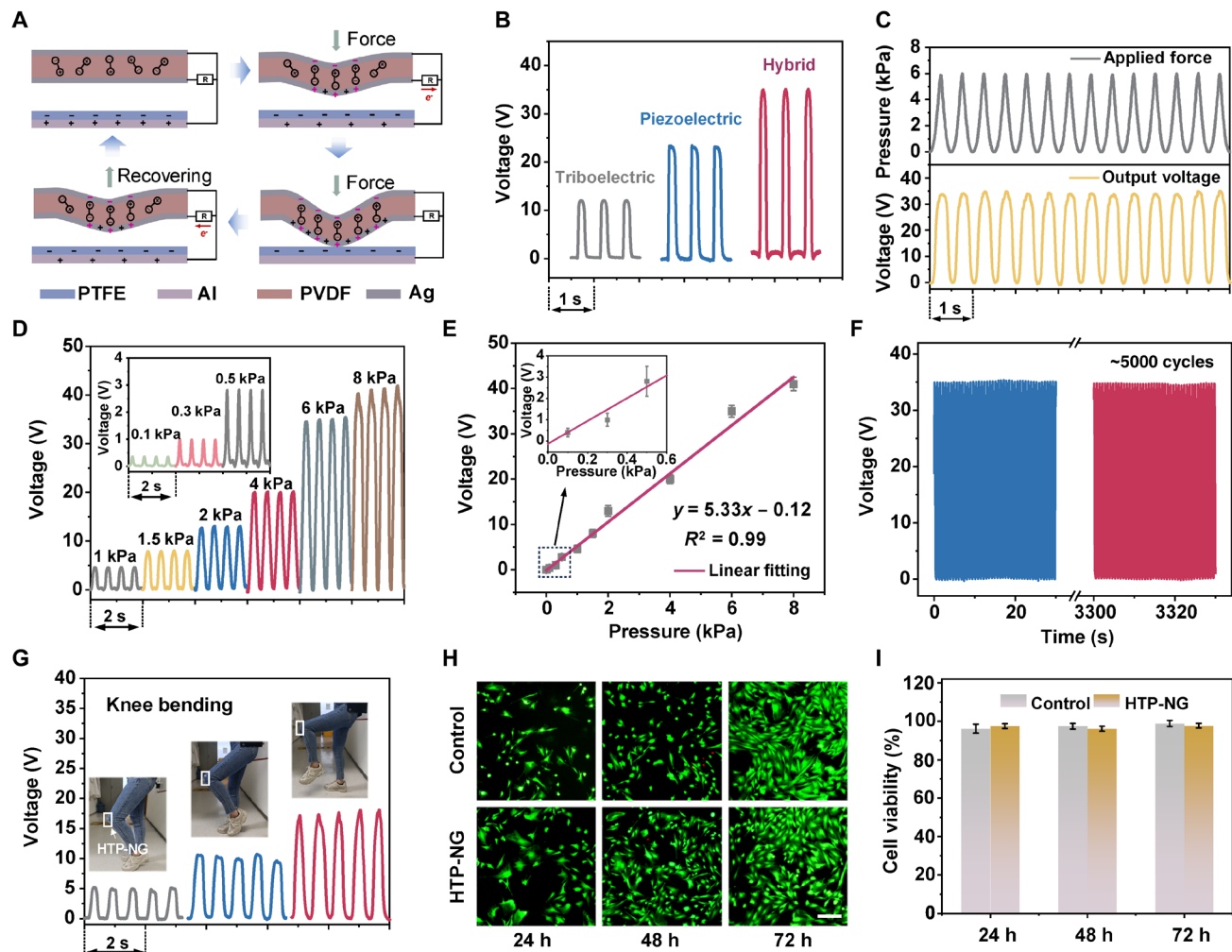


Fig. 2. Electrical performance and biocompatibility of HTP-NG. (A) Schematic depicting the operational principle of HTP-NG, converting applied force into real-time electron flow within the external circuit. (B) Voltage signals generated by the triboelectric module, piezoelectric module, and hybrid module of the HTP-NG. (C) The applied pressure (~ 6 kPa) and output voltage of the HTP-NG were monitored in real time. (D) Output voltage signals under different pressures. The inset shows the output voltage signals of HTP-NG under low pressures (≤ 0.5 kPa). (E) Linear fitting of peak-to-peak voltage and pressure change ($n = 3$). The inset shows an enlarged fitting curve for the output voltage signals of HTP-NG at low pressures (≤ 0.5 kPa). (F) Long-term stability test of HTP-NG. (G) Output voltage of HTP-NG in response to knee bending. (H) Fluorescence images of stained BMSCs that were cultured in a regular cell culture dish (top) and on HTP-NG (bottom). Scale bar, 100 μm . (I) Normalized viability of BMSCs after being cultured for 3 days. Data are expressed as means \pm SD. One-way ANOVA with Tukey's multiple comparisons test, not significant, $n = 3$. The working area of HTP-NG was set to 1 cm^2 , and the pressure was 6 kPa unless otherwise specified.

the HTP-NG to illuminate ~ 145 light-emitting diodes (LEDs) (fig. S8B). The excellent output power endowed the HTP-NG with sufficient charge transfer capacity to charge capacitors (figs. S9 and S10). Moreover, the comparison between HTP-NG and current hybrid NGs (as summarized in table S4) also demonstrated that the HTP-NG offered a notable advantage due to its highly effective electromechanical conversion performance (41–43).

The electromechanical conversion capacity of the HTP-NG in response to joint movements from the human body system was evaluated before implantation *in vivo*. The HTP-NG device was fixed to volunteers at the skin surface corresponding to the different joints (Fig. 2G and fig. S11). It was found that the HTP-NG displayed high sensitivity to the external force stimulated by joint motions. Moreover, the electric pulse signal produced was directly

related to the frequency and amplitude of joint motions, indicating the great potential of implantable HTP-NG for biofeedback ES therapy. In addition, we also carried out an accelerated fatigue test in phosphate-buffered saline (PBS) solution to investigate the durability of HTP-NG in a liquid state (mimicking the *in vivo* environment). It could be seen that the HTP-NG had a stable electrical output performance even when immersed in PBS solution for 2 weeks (fig. S12). The excellent stability of the HTP-NG in the liquid state could be primarily attributed to the strong encapsulation layer, which avoided liquid leakage. In addition, biocompatibility of the HTP-NG was essential to avoid rejection by biological tissues after implantation. Rat bone marrow stem cells (BMSCs) exhibited favorable adhesion and spreading behavior on the above encapsulation layer material and on a regular cell culture dish (Fig. 2H). The

quantification of the percentage of live cells showed that the cell viability of the experimental group was similar to that of the control group at each time point (Fig. 2I). The good cell morphology and proliferation on the encapsulation layer indicated that the HTP-NG device was noncytotoxic and biocompatible.

Fabrication and characterization of EABP conductive hydrogel

The conductive hydrogel was prepared using ECM grafted with AlgMA and BP@PDA (Fig. 3A). BP nanosheets were first prepared by ultrasonic exfoliation of bulk BP, and the BP nanosheets were then immersed into a dopamine solution to form BP@PDA. The optical images showed the difference in color between BP and BP@PDA (fig. S13). Transmission electron microscopy (TEM) images and their diffraction pattern showed the typical sizes of BP nanosheets with a typical few-layer and amorphous structure (fig. S14A). The atomic force microscopy (AFM) image displays the height profile as marked by the red line, indicating the ultrathin structure of BP nanosheets with only 1.175 nm (fig. S14B). Elemental analysis from TEM displayed the distribution of nitrogen (N), oxygen (O), and phosphorus (P) on the surface of BP nanosheets, indicating the successful modification of the BP nanosheets with PDA (fig. S14C). In addition, the ultraviolet-visible (UV-Vis) spectra of BP and BP@PDA were also different (fig. S15A), and the UV-Vis spectra with different concentrations of BP@PDA measured at 280 nm were used to create a standard curve for further use (fig. S17). In the Fourier transform infrared (FTIR) spectrum of BP, the adsorption peak at $\sim 1642\text{ cm}^{-1}$ represents the P=O stretching vibration (44). After PDA modification, the peak at $\sim 1510\text{ cm}^{-1}$ can be assigned to the bending vibrations of N-H in PDA (45). The FTIR spectra showed that PDA was coated successfully onto the surface of BP nanosheets (fig. S15B). In addition, the zeta potential of BP nanosheets was -28.7 mV and increased to -8.1 mV after modification with PDA (fig. S16A), and a slightly negative charge would be appropriate for nanosheet dispersibility and cell accessibility (46). The diameter measured by dynamic light scattering (DLS) was approximately 200 nm, which could provide a sufficiently large surface for current passing (fig. S16B). The stability of BP and BP@PDA was also evaluated by UV-Vis on days 1, 3, 7, 14, and 21. During this period, the absorbance intensity of the BP solution decreased gradually after exposure to air, while the absorbance intensity of BP@PDA showed no substantial change, indicating that the PDA coating greatly enhanced the stability of BP nanosheets against oxygen attack (fig. S18).

To increase the biocompatibility of hydrogel, ECM was prepared as previously described (47). Histological images, including hematoxylin and eosin (H&E) staining, Masson staining, Oil Red O staining, and 4',6-diamidino-2-phenylindole (DAPI) staining, demonstrated the successful decellularization of adipose tissue (fig. S19A), and a high efficiency of decellularization was verified by quantification of DNA content (fig. S19B). The resulting ECM was further used to prepare the EA and EABP composite hydrogels as described in Materials and Methods. Scanning electron microscopy (SEM) analysis revealed the porous structure of the EABP hydrogel (Fig. 3C), which would allow the efficient diffusion of nutrients and oxygen for tissue repair (48). The influence of the concentration of BP@PDA in the hydrogel on the viscoelasticity of the EA hydrogel was evaluated through rheological characterization. After the addition of BP@PDA, EABP-100 exhibited the highest viscosity, while the lowest

viscosity was observed in EABP-400, which may be due to excessive BP@PDA decreasing the overall stability of EA (fig. S20B). The G' values were larger than the G'' values at the initial period, suggesting that a hydrogel was successfully formed. When the shear stress exceeded 196 Pa, the G' values of EABP-100 notably decreased to generate a crossover point, indicating the collapse of the hydrogel network. However, the G' values of EA and EABP-400 were 11.9 and 14.3 Pa, respectively, which were much smaller than those of EABP-100 (fig. S20A). These rheological results demonstrated that EABP-100 had a stable structure. The incorporation of an appropriate amount of BP@PDA improved the stability of the hydrogel because of the formation of peptide bonds between the amino groups of BP@PDA and the carboxyl groups of EA (49). In addition, the ECM, together with BP@PDA and AlgMA, could also form hydrogen bonds by intra- and intermolecular hydrogen bonds (Fig. 3, A and B). Thus, the interaction of BP@PDA and EA resulted in improved mechanical properties. Compared to the EABP-100 hydrogel, the stability of the EABP-400 hydrogel decreased, which may be due to the excessive concentration of BP@PDA forming aggregates, leading to phase separation of the suspension, which disrupted the hydrogel network (50, 51). To further evaluate the adhesive property of the EABP-100 hydrogel, the cured hydrogel was placed in finger contact with different materials, including plastic, glass, metal, and skin. The results showed that the hydrogel could adhere to these materials well (fig. S21). The lap shear test also demonstrated the increased adhesive property of the EABP-100 hydrogel compared with the EA hydrogel (fig. S22). In addition, the swelling property is one of the most important parameters of hydrogels for their application. After incubation in PBS for 24 hours, all the hydrogels showed excellent water absorption capacity without a significant difference, although a slight reduction in the swelling ratio was displayed in the EABP-400 hydrogel (fig. S23A). In the enzymatic degradation test (fig. S23B), these hydrogels could be degraded within 1 month and showed no significant difference, which would provide a window period to favor ES. Meanwhile, the conductivity of EA and EABP hydrogels was also evaluated. An increasing conductivity of the hydrogel was observed with increasing concentrations of BP@PDA (Fig. 3D). LED was also successfully lit when a small voltage was applied to EABP-100 (movie S1). The good electrical conductivity of the EABP hydrogel could be attributed to the current passing through the bridging BP@PDA nanosheets.

Biocompatibility and proliferation evaluation of conductive hydrogels

First, live/dead staining was applied to evaluate the biocompatibility of conductive hydrogels, and the ES process on BMSCs was presented as schematic illustration (Fig. 3E). Voltage generated from the HTP-NG could be regulated by adjusting the frequency of the reciprocating motor and the distance between the reciprocating motor's force arm and the fixed HTP-NG to maintain relative consistency with the output in vivo. A high percentage of the cells survived after being treated with or without ES in the EA and EABP-100 groups, while a high percentage of cells died in the EABP-400 group with or without ES (Fig. 3F and fig. S24), which demonstrated that EABP-100 had better cytocompatibility and was more appropriate for the following biological experiments combined with its good performance in the conductive and rheological tests. If not specifically indicated, EABP represents EABP-100 in the following experiments. To further explore the proliferation of BMSCs, cells were

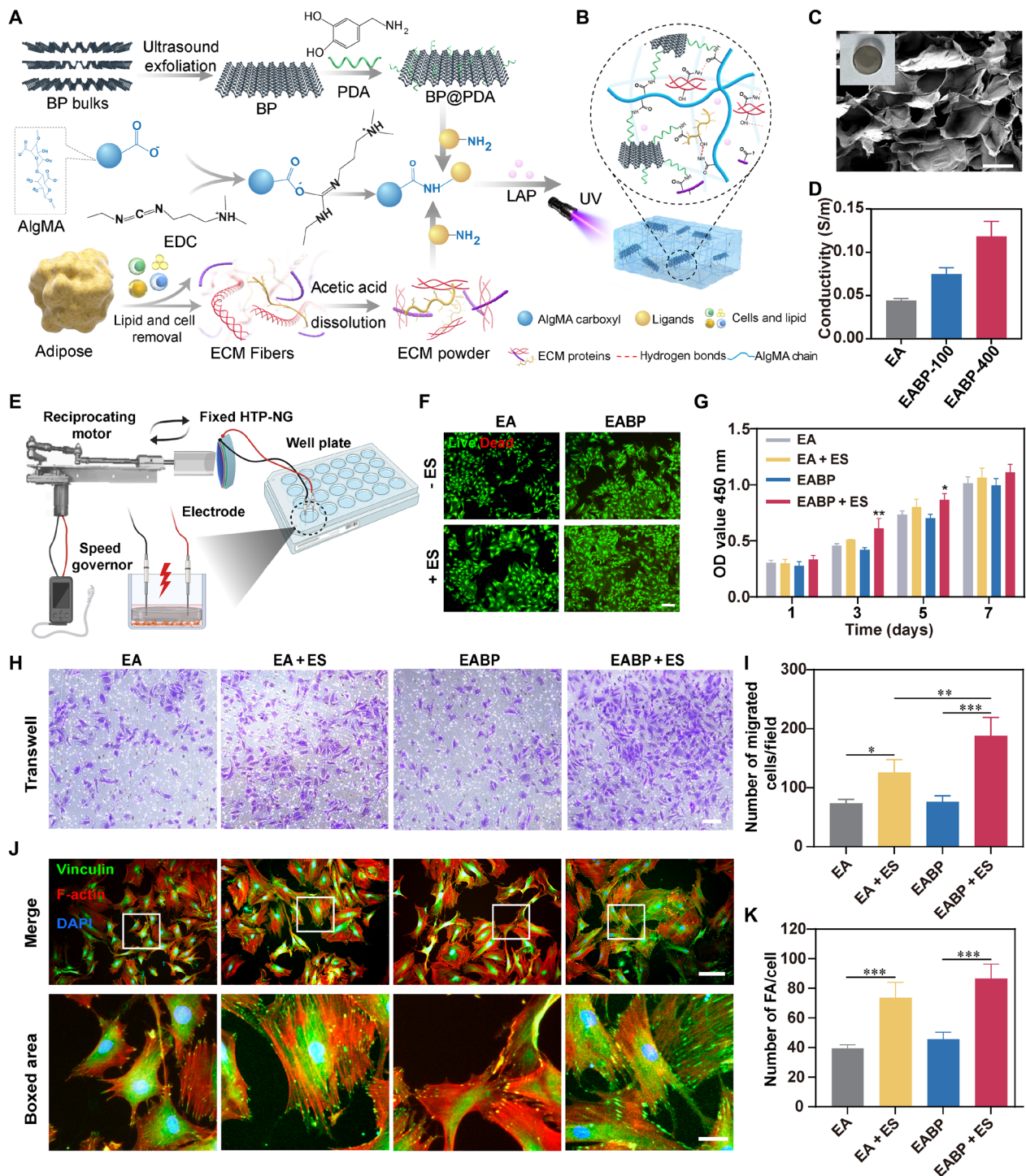


Fig. 3. Schematic illustration of the formation of EABP conductive hydrogels and the cytocompatibility of the BD-ES system on BMSCs. (A) Schematic illustration of the preparation of EABP conductive hydrogels. (B) Schematic illustration of the formation of crosslinked EABP hydrogel. (C) UV-cured EABP hydrogel and SEM image. Scale bar, 100 μm . (D) Conductivity of EA and EABP hydrogels. Data are expressed as means \pm SD, one-way ANOVA with Tukey's multiple comparisons test, not significant, $n = 3$. (E) Schematic illustration of the stimulation on BMSCs by BD-ES system, created with BioRender.com. (F) Live/dead staining of BMSCs cultured with EA or EABP hydrogels with or without stimulation of BD-ES system. Scale bar, 300 μm . (G) Cell viability of BMSCs cultured with EA or EABP hydrogels with or without stimulation of BD-ES system. Asterisk indicates statistical significance compared to the EA group. Data are expressed as means \pm SD, one-way ANOVA with Tukey's multiple comparisons test, $^{**}P < 0.01$ and $^{*}P < 0.05$, $n = 3$. (H) Images of migrated BMSCs stained with crystal violet in Transwell assay. Scale bar, 200 μm . (I) Statistical analysis of the number of migrated cells. Asterisk indicates statistical significance between groups. Data are expressed as means \pm SD, one-way ANOVA with Tukey's multiple comparisons test, $^{***}P < 0.001$, $^{**}P < 0.01$, and $^{*}P < 0.05$, $n = 3$. (J) Immunofluorescence staining of cellular F-actin (red), nuclei (blue), and vinculin focal staining (green). Scale bars, 200 and 40 μm . (K) Quantification of the number of focal adhesions (FAs). $^{***}P < 0.001$, $n = 3$. All data are expressed as means \pm SD.

cocultured with hydrogels for 7 days. No significant difference was observed among the four groups on days 1 and 7, although the EABP + ES group maintained a slightly higher proliferation rate than the other groups. The incorporation of BP@PDA in EA did not inhibit cell growth, indicating that EABP had great biocompatibility. Moreover, BMSCs cocultured with EABP under ES significantly differed from the EA group at both day 3 and day 5 (Fig. 3G), indicating that the conductive hydrogel could promote cell proliferation via ES. Next, BMSC migration in the EA and EABP groups with or without ES by HTP-NG was examined using Transwell plates (8- μ m pore size). After stimulation for 1 hour using a homemade ES system (fig. S25), the groups with ES displayed more BMSC migration than the other groups without ES (Fig. 3H). In particular, the EABP hydrogel significantly enhanced BMSC migration with ES compared with the other groups (Fig. 3I). In addition, cells cocultured without ES exhibited limited spreading and distribution of vinculin. In contrast, much more focal adhesion expression in the EABP + ES group marked by vinculin-fluorescein isothiocyanate (FITC) demonstrated that the conductive hydrogel with ES could strongly promote cell adhesion (Fig. 3J). These findings demonstrated that EABP notably facilitates cell proliferation, migration, and adhesion under ES.

To further evaluate the feasibility of our proposed method *in vivo*, a hemolysis assay was then carried out to evaluate the biocompatibility of conductive hydrogels. After incubation with EA or EABP hydrogel for 4 hours, the human red blood suspension showed less than a 5% hemolysis degree, indicating good biocompatibility of the hydrogels (fig. S27). To further evaluate the biocompatibility of hydrogels and cell infiltration *in vivo*, sterilized hydrogels were implanted subcutaneously in Sprague-Dawley rats, and H&E staining was performed on days 7 and 14 (fig. S28, A and B). H&E staining on day 7 revealed visible infiltration of inflammatory cells around the hydrogels. However, the number of inflammatory cells remarkably decreased in the surrounding scaffold on day 14, and most infiltrated cells could be observed in the hydrogels, indicating that these hydrogels had good cellular compatibility. In particular, the section of explant showed a less distinct interface between the EABP conductive hydrogel and surrounding tissue after 14 days, which strongly indicated that the EABP hydrogel facilitated integration with the surrounding tissue via cell migration and recruitment. The good integration of the conductive hydrogel could be attributed to dopamine-induced cell adhesion (52). Cell adhesion capacity and biocompatibility could be enhanced by dopamine-modified scaffolds via the activation of integrin, which has been proved by many studies (53, 54). As a result, the EABP displayed good biocompatibility and integrated well with the surrounding tissue.

Investigation of osteogenic differentiation and intracellular calcium ion level

Osteogenic differentiation of BMSCs induced by EA and EABP with or without ES was examined. Significantly stronger positive alkaline phosphatase (ALP) staining was observed in the EABP + ES group on days 7 and 14 (Fig. 4, A and B). In addition, alizarin red S staining revealed more mineral deposition in the ES+ groups (Fig. 4C). Significantly more alizarin red colonies were observed in the EABP + ES group than in the other groups (Fig. 4D). These results demonstrated that the conductive hydrogel could promote the osteogenic differentiation of BMSCs under ES. The changes in intracellular calcium concentration were further analyzed. ES can activate calcium channels within the cell membrane to induce calcium influx and the

release of calcium from the intracellular calcium pool (55). As a secondary messenger, calcium is involved in multiple signal transduction pathways related to osteogenic differentiation (56), and the calcium probe Fluo-4 AM was used to measure intracellular calcium (57). The Fluo-4 AM fluorescence intensity was stronger in the groups with ES. The BMSCs treated with EABP under ES significantly differed from the other groups (fig. S26, A and B). The intracellular calcium concentration of BMSCs was further analyzed by flow cytometry after stimulation for different times. The results demonstrated that the intracellular calcium level increased with increasing stimulation time (fig. S26C).

Mechanism exploration of osteogenic-related pathways involving biological process and signal transduction of BMSCs

To explore the underlying mechanism of osteogenesis under different conditions, RNA sequencing (RNA-seq) of BMSCs cultured with or without ES for 7 days was performed. Gene expression levels were quantified using fragments per kilobase per million mapped fragments (FPKM) (58). The results showed no batch effect between the two sample groups (Fig. 5A). In addition, principal components analysis (PCA) illustrated the variances in gene expression in BMSCs cultured with or without ES between the control and EABP + ES groups (Fig. 5B). The volcano plot and heatmap showed a total of 351 differentially expressed genes (DEGs) identified by comparison of the control and EABP + ES groups, including 163 up-regulated genes and 188 down-regulated genes (Fig. 5, C and D). On the basis of the results of Gene Ontology (GO) analysis, DEGs were enriched in biological processes related to the regulation of angiogenesis, skeletal system development, and axon development. ES also altered cellular components and molecular functions, including ECM, collagen-containing, and signaling receptor regulator activity (Fig. 5E). Moreover, Kyoto Encyclopedia of Genes and Genomes (KEGG) pathway analysis was performed to further investigate the DEGs to reveal the possible underlying osteogenic signaling pathways in which they were enriched. Among these pathways, PI3K-AKT, which is involved in osteogenesis, was notably affected by ES (Fig. 5G and fig. S29). PI3K-AKT is an important intracellular pathway that can regulate cell survival, proliferation, protein synthesis, and other cell activities. The importance of PI3K-AKT pathway on osteogenesis has been proved by some studies (59, 60), and the expression of PI3K and AKT protein was up-regulated under ES as proved by Western blot analysis (Fig. 5L). Moreover, gene set enrichment analysis (GSEA) found that the mechanosensitive proteins of PIEZO1 and PIEZO2 were up-regulated, indicating that ES may exhibit positive influence on osteogenesis by up-regulating the response of BMSCs to mechanical stimulus (Fig. 5F). In the EABP + ES group, the WNT and MAPK pathway (Fig. 5, H and I, and fig. S30A), which is closely associated with osteogenesis, was also found to remain highly relevant. PIK3CA, WNT11, and extracellular signal-regulated kinase 1 (ERK1) proteins were still found to be highly expressed in biological processes involving cellular responses to mechanosensitive stimuli, suggesting a potential synergistic effect of these signaling pathways with mechanosensitive stimulus responses. Moreover, the positive regulation of osteoblast differentiation by RUNX2, positive calcium ion transport, and calcium ion import activities were also enhanced in the EABP + ES group (Fig. 5, J and K, and fig. S30, B to D). The biological process of positive calcium ion regulation was enhanced under ES, which would increase cellular calcium ion

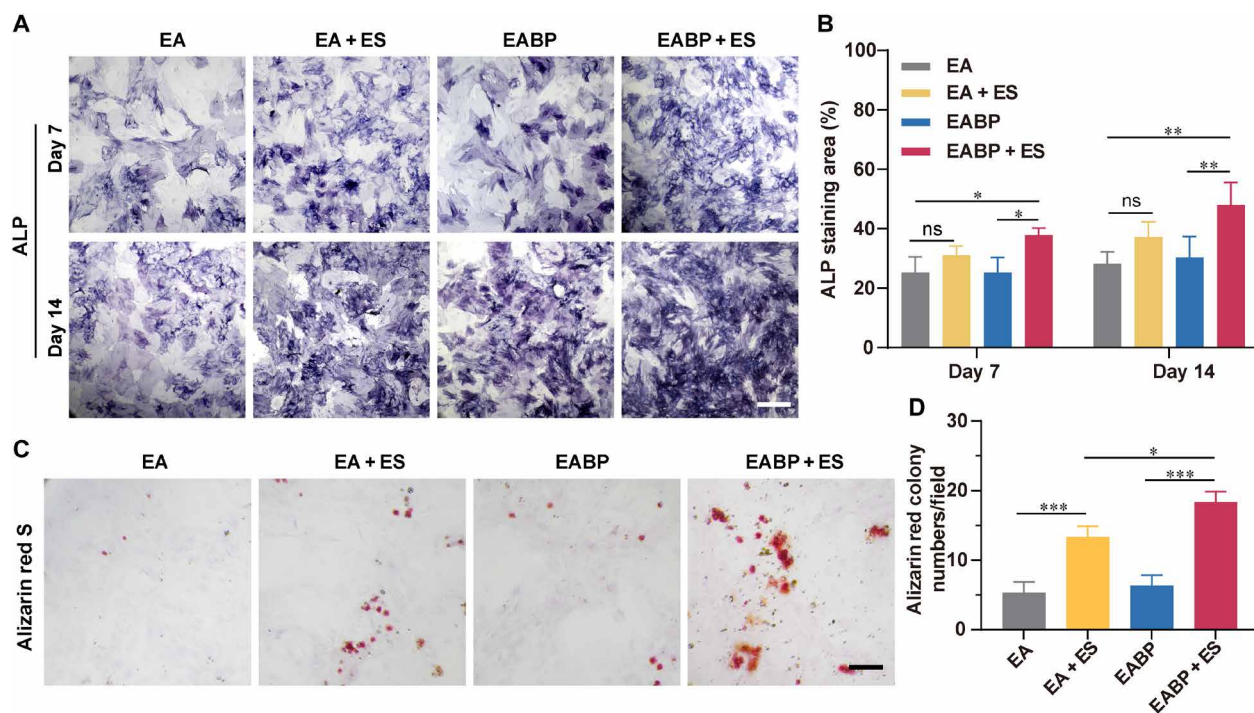


Fig. 4. Osteogenic differentiation of BMSCs evaluated by ALP and alizarin red staining under BD-ES system stimulation. (A) ALP staining of BMSCs cultured with or without BD-ES system stimulation at days 7 and 14. Scale bar, 500 μ m. (B) Quantitative evaluation of the ALP-positive area on days 7 and 14. Data are expressed as means \pm SD. One-way ANOVA with Tukey's multiple comparisons test, $**P < 0.01$ and $*P < 0.05$, $n = 3$. (C) Alizarin red staining of BMSCs on day 21. (D) Quantitative evaluation of calcium nodules in alizarin red staining on day 21. Scale bar, 200 μ m. Data are expressed as means \pm SD, two-way ANOVA with Tukey's multiple comparisons test, $***P < 0.001$ and $*P < 0.05$, $n = 3$.

concentration to promote calcium deposition and osteogenesis (61). Western blot and polymerase chain reaction (PCR) verified the high expression level of key osteogenesis-related genes in the EABP + ES group (Fig. 5L and fig. S31). These results revealed the activation of osteogenesis-related biological processes under ES by the BD-ES system, which may explain why BMSCs displayed increased mineralization potential under ES, as displayed above.

Performance of conductive hydrogels in promoting bone regeneration

Encouraged by the above results, the therapeutic effect of conductive hydrogels connected with the HTP-NG system in the promotion of bone repair was further studied in vivo, and the timeline was shown in fig. S32. Briefly, to construct the BD-ES system, sterile HTP-NG was first placed in front of the knee joint through a small incision (Fig. 6A and fig. S34A). A cylindrical defect 3 mm in diameter was then drilled in the medial condyle of the other femur, and the proximal and distal ends of the HTP-NG were connected to the femoral defect using subcutaneously embedded platinum (Pt) soft wires. The Pt electrodes (0.1 mm) were embedded in the conductive hydrogel, and the spacing of the exposed Pt electrodes surface was 1.5 mm and the length was 3 mm as shown in fig. S33. To assess the biocompatibility of HTP-NG in vivo, H&E staining of the surrounding tissue was performed 2 weeks after implantation, and no difference was found in the tissue surrounding the HTP-NG and normal tissue (figs. S34B and S35), indicating that HTP-NG has good biocompatibility. Computed tomography (CT) scans performed 2 weeks after surgery showed that the HTP-NG was still located in front of

the knee without displacement after exercise in the cage (Fig. 6B). In addition, the HTP-NG could efficiently harvest energy from knee joint movements of a rat and synchronously produce a biphasic electric pulse signal after implantation for 2 weeks (Fig. 6, C and D; fig. S36; and movie S2), and the voltage output varied based on the degree of knee flexion (fig. S37). These results demonstrated that the BD-ES system connected with the conductive hydrogel had great potential for application in vivo. While current self-powered biomedical devices have primarily focused on wound healing (62, 63), nerve stimulation (64–67), and cardiac pacing (68, 69), the HTP-NG has the potential to achieve a broader range of stimulus signals to accelerate bone regeneration (table S5). To further investigate the osteogenic properties in vivo, we constructed BD models injected with the conductive hydrogel in Sprague-Dawley rats at the medial femoral condyle and implanted the BD-ES system. To generate electric field from the BD-ES system, rats with well-healed incisions (movie S3) and in which the BD-ES system remained well connected without displacement after 4 weeks of exercise (fig. S38) were subjected to running on a treadmill run at a speed of 1 km/hour for 30 min daily for another 4 weeks.

To evaluate bone regeneration under the BD-ES system, rats with the same femoral defect and exercise regime as described above were used as a control group. As shown in the micro-CT images, the three-dimensional (3D) reconstruction and sagittal and transverse planes of the defect area displayed a better osteogenic induction effect in the EABP + ES group than in the other groups (Fig. 6E). Furthermore, to quantify bone regeneration, morphological parameters, including bone mineral density (BMD), bone volume (BV)/

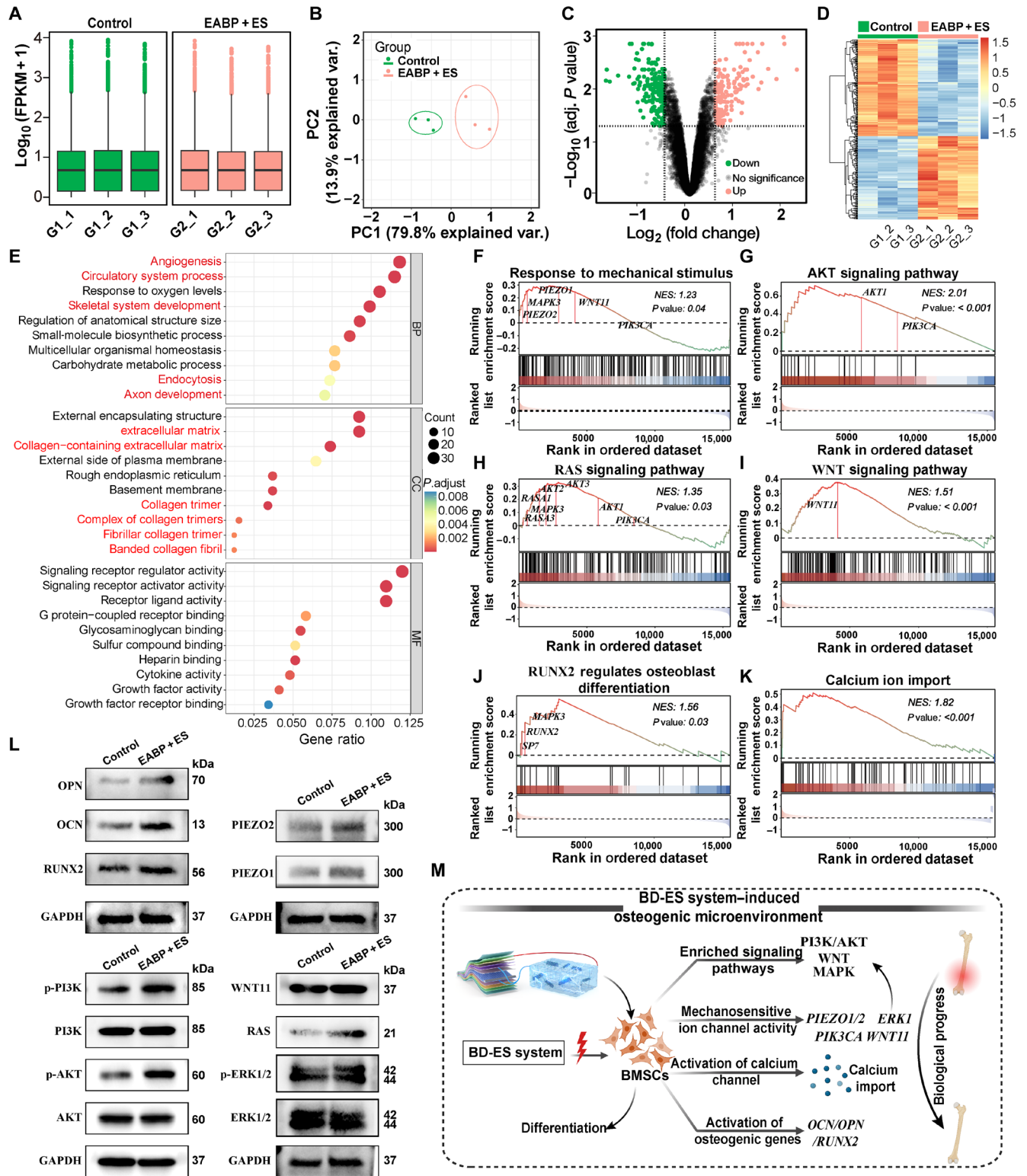


Fig. 5. Exploration of gene expression patterns and functional enrichment analysis. (A) Box plot depicting FPKM values. (B) PCA illustrating the variance between the control and EABP + ES groups. (C and D) Volcano plot and heatmap showing the DEGs, including those that are up-regulated (red dots) and down-regulated (green dots). (E) GO enrichment analysis including BP (biological process), CC (cellular component), and MF (molecular function). (F to K) GSEA of osteogenesis-related signaling pathways and biological processes. (L) Western blot analysis of the expression of core proteins involved in osteogenic, mechanosensitive, and enriched signaling pathways between the control (Ctrl) group and EABP + ES group. (M) Schematic view of the possible mechanism involved in the osteogenesis process based on transcriptome sequencing results.

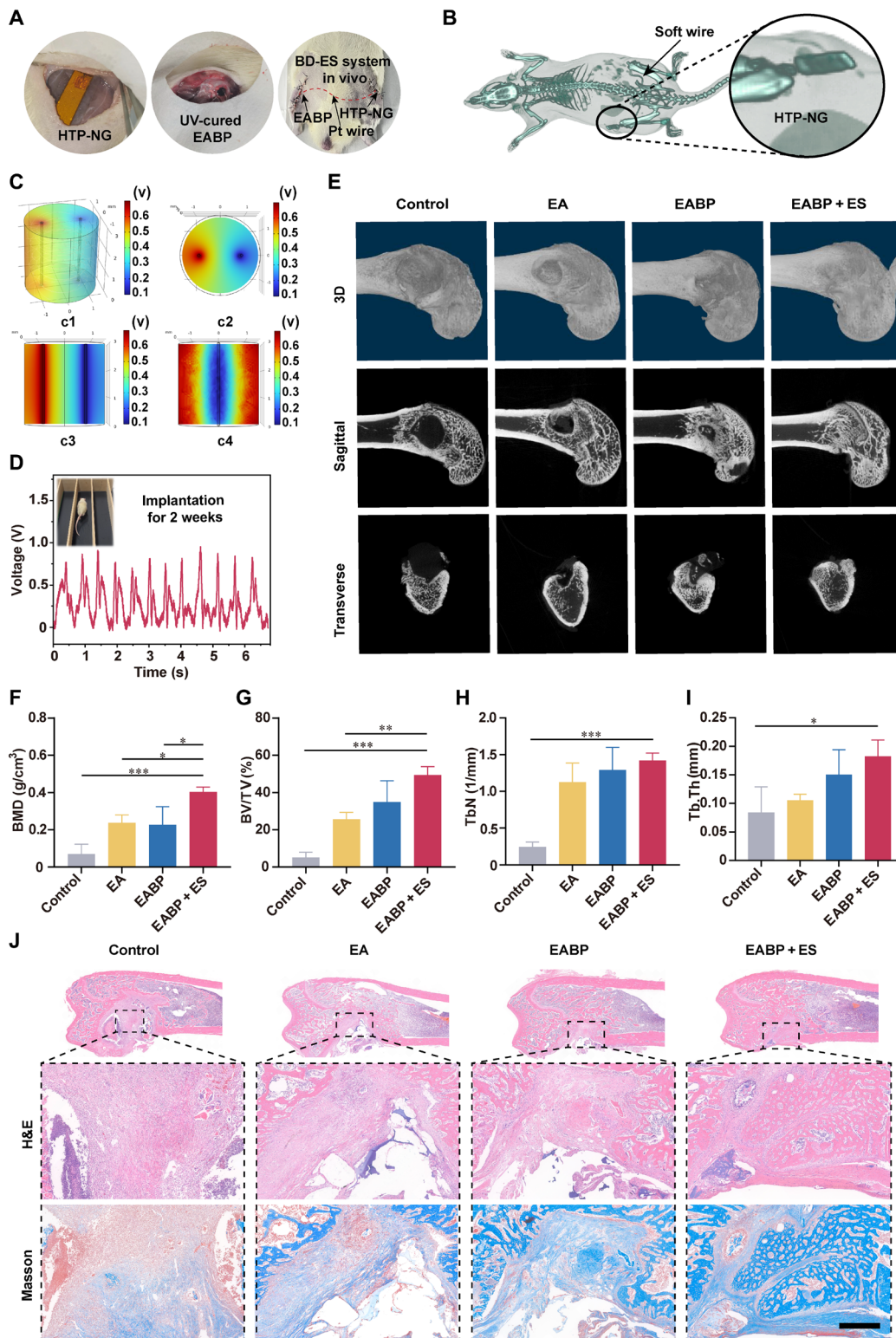


Fig. 6. The implantation of the BD-ES system in vivo and its ability to promote bone regeneration were evaluated by micro-CT and histochemical staining of femoral samples. (A) Surgical images of the implanted BD-ES system. **(B)** 3D reconstructive CT images of the BD-ES system 2 weeks after surgery. **(C)** Distribution of the electric potential in the EABP conductive hydrogel from HTP-NG calculated from finite element analysis. **(D)** The output voltage of HTP-NG in vivo when Sprague-Dawley rats run at a speed of 1 km/hour 2 weeks after surgery. **(E)** 3D reconstruction images and sagittal and transverse view images of the distal femur by micro-CT. **(F to I)** Micro-CT quantitative evaluation of BMD, BV/TV, Tb.N, and Tb.Th in defect areas. Data are expressed as means \pm SD. One-way ANOVA with Tukey's multiple comparisons test, *** $P < 0.001$ and * $P < 0.05$, $n = 3$. **(J)** H&E and Masson's trichrome staining images of the rat femurs. Scale bar, 500 μ m.

total volume (TV), trabecular number (Tb.N), and trabecular thickness (Tb.Th), were analyzed. A significant amount of regenerated bone was observed in the EABP + ES group compared with the other groups (Fig. 6F). The BV/TV value of the EABP + ES group significantly differed from that of the control and EA groups and was 1.4-fold higher than that of the EABP group (Fig. 6G). The results of Tb.N and Tb.Th also significantly differed between the EABP + ES group and the control group (Fig. 6, H and I). Specifically, H&E and Masson trichrome staining showed much more newly formed bone and collagen distribution in the EABP + ES group than in the other three groups (Fig. 6J). In addition, the results of immunohistochemical staining displayed much more type I collagen deposited in the EABP + ES group (Fig. 7A). Immunofluorescence staining showed that the expression of CD31 and alpha-smooth muscle actin (α -SMA) was increased, with more angiogenesis noted in the EABP + ES group (Fig. 7B), and a significant difference in the new vessel density could be observed in the EABP + ES group (Fig. 7C). Sustained blood flow is required for cell survival, transport of nutrients, and removal of cellular metabolites, which would facilitate osteoblast function, including proliferation, differentiation, and bone formation (70). Moreover, notably increased expression of osteogenesis-related proteins (OCN, OPN, and RUNX2) was observed in the EABP + ES group by immunofluorescence staining (Fig. 7, D to F, and fig. S39). In addition, lower expression of the inflammatory cytokines interleukin-6 (IL-6) and tumor necrosis factor- α (TNF- α) was observed at 6 weeks in the EABP + ES group (fig. S40), indicating optimal biocompatibility. The H&E staining of internal organs, including the heart, liver, spleen, lung, and kidney, showed no difference compared with the control group (fig. S41), which further supports the good biocompatibility of the BD-ES system *in vivo*. In summary, these results demonstrated that the conductive hydrogel with HTP-NG system implantation could greatly facilitate collagen deposition and angiogenesis to support bone generation.

DISCUSSION

ES, as an imperative biophysical level regulator and nonpharmacological intervention, has received considerable attention for its potential to augment the regenerative process to accelerate bone repair. Here, we designed and fabricated a self-powered BD-ES system based on an HTP-NG and a conductive EABP hydrogel for the repair of BDs. Compared to conventional ES devices, the fabricated HTP-NG can efficiently harvest energy from rat knee joint movements and synchronously produce a biphasic electric pulse signal, which eliminates the need for a cumbersome electrical stimulator with complex operation and the potential for additional electric injury. High-efficiency energy conversion and remarkable output performance provide a solid basis for the prospective biomedical application of this flexible HTP-NG. Furthermore, we also developed a conductive multifunctional hydrogel by incorporating 2D BP nanosheets and ECM into the AlgMA hydrogel matrix for electroactive tissue repair.

In vitro, the BD-ES system accelerated BMSC proliferation and migration. In addition, osteogenic differentiation was greatly enhanced by BD-ES system stimulation with remarkable calcium influx, ALP-positive staining, and more calcium nodules. Biological processes, including angiogenesis, skeletal system development, and connective tissue development, were also enhanced. Meanwhile, the

BD-ES system advanced a bone regenerative process with increased expression of osteogenesis-related proteins *in vivo*. Moreover, transcriptome sequencing revealed that the BD-ES system could up-regulate the expression of several proteins in response to mechanical stimuli involving the PI3K/AKT, WNT, and MAPK signaling pathways. Moreover, GSEA revealed that the mechanosensitive proteins PIEZO1 and PIEZO2 were up-regulated, indicating that ES may have a positive influence on osteogenesis by up-regulating the response of BMSCs to mechanical stimuli. These results revealed that ES may act synergistically with mechanical stimulation in altering the expression of proteins to support bone regeneration.

Bone has been reported to generate electrical signals when mechanical stress is applied, which can accelerate bone repair in the absence of exogenous growth factors (71, 72). The osteogenic outcomes observed *in vitro* and bone healing observed *in vivo* in this study demonstrated that the conductive hydrogel could better accelerate bone regeneration by combining only the electric pulse signal generated from the HTP-NG. In addition, we have effectively combined the rehabilitative functional exercises emphasized in the clinic with the BD-ES system, which is of great significance for the treatment of patients with clinical BDs. In particular, by regulating the amplitude or frequency of the patient's joint movement after *in vivo* implantation, the produced electrical signals can be easily controlled for accelerating tissue regeneration.

There are several limitations to this study. The size of HTP-NG can be further minimized, and additional optimization will also be needed to enable remote monitoring of voltage output under rehabilitation for clinical application. It is also a practical challenge concerning the removal of the device after healing. Owing to the development of materials science, biodegradable electromechanical devices are gaining more and more attention (11). They can be degraded and absorbed gradually *in vivo* without removal, avoiding secondary surgery, making them an outstanding power source candidate for transient *in vivo* medical devices (73). In addition, some biodegradable piezoelectric polymers and natural materials are also a new trend for developing electromechanical devices, which are different from the conventional materials with concerns of biosafety and biocompatibility. Specifically, piezoelectric biomaterials like collagen amino acids are mostly biodegradable *in vivo*, showing great potential in the development of transient implantable electromechanical devices (74, 75), and designing high-performance and biodegraded piezoelectric biomaterials is a potential strategy to realize the application of implantable electrostimulation device without removal of the device after healing. In addition, transcriptome sequencing revealed that several proteins that respond to mechanical stimuli were up-regulated under ES from the BD-ES system. Therefore, it is necessary to further investigate the cellular and molecular mechanisms through which ES promotes osteogenesis, which will be of great value in realizing clinical precision therapy at the cellular and molecular levels.

In summary, we developed a self-powered BD-ES system that consisted of a flexible HTP-NG and a conductive EABP hydrogel. Through seamless system integration and functional optimization, this fully implantable BD-ES system is capable of greatly accelerating the repair of BDs and shows potential to be applied in the clinic in combination with the necessary rehabilitation exercise to promote bone repair. The BD-ES system demonstrated here offers new insight into the design of a self-responsive closed-loop ES platform and presents a new pathway for future intelligent health care.

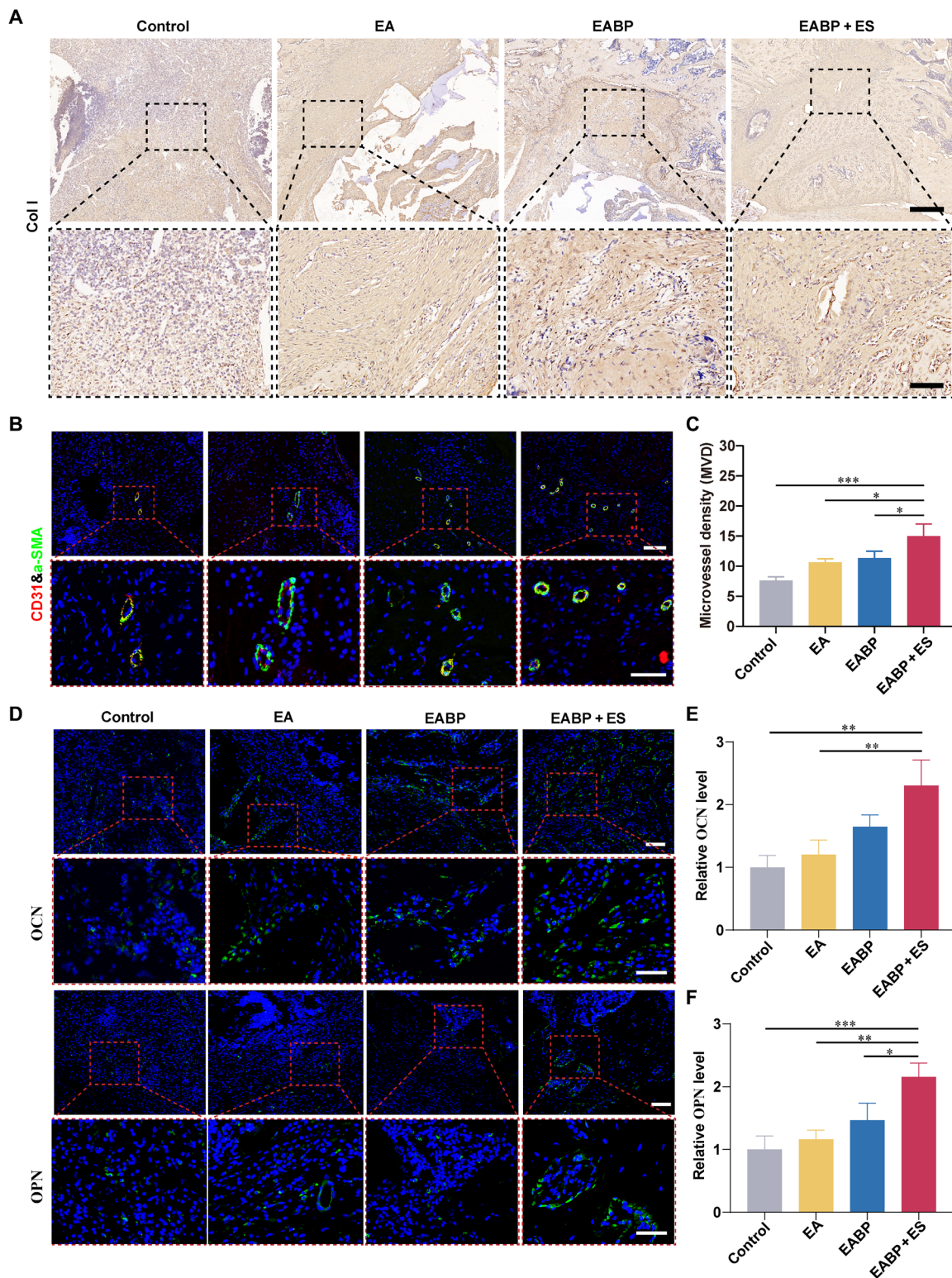


Fig. 7. Immunohistochemical and immunofluorescence staining images and relative quantitative analysis of angiogenesis- and osteogenesis-related markers. (A) Immunohistochemical staining of type I collagen. Scale bars, 400 and 100 μm . (B) Immunofluorescence staining for CD31 (red) and α -SMA (green). Scale bars, 100 and 50 μm . (C) Quantification of MVD based on the results of CD31 and α -SMA staining. Data are expressed as means \pm SD. One-way ANOVA with Tukey's multiple comparisons test, *** $P < 0.001$ and * $P < 0.05$, $n = 3$. (D) Immunofluorescent detection of osteogenesis-related proteins (OCN and OPN). Scale bars, 100 and 50 μm . (E and F) Quantitative expression of OCN and OPN. Data are expressed as means \pm SD. One-way ANOVA with Tukey's multiple comparisons test, *** $P < 0.001$, ** $P < 0.01$, and * $P < 0.05$, $n = 3$.

MATERIALS AND METHODS**Fabrication of HTP-NG**

A commercial poled PVDF film coated with an Ag electrode on both sides (110 μm , Measurement Specialties Inc.) was used as the piezoelectric material. The PVDF film with a required size (0.5 cm \times 2 cm) was attached to a thin Kapton film (100 μm) for the construction of the piezoelectric layer. In contrast, we selected a nanostructured PTFE film, which was surface-activated by an inductively coupled plasma etching system and adhered to a Kapton film linked with a conductive aluminum foil to serve as the triboelectric layer. For assembling HTP-NG, an acrylic layer with a thickness of 0.8 mm was used as a spacer between adjacent triboelectric layers to ensure electrical disconnection. Afterward, a Teflon film was used as the first packaging layer to encapsulate the assembled HTP-NG. Last, PDMS (Sylgard 184 silicone rubber, Dow Corning) was covered on the surface of the device as the second package layer for fabricating a fully encapsulated HTP-NG.

Preparation of BP nanosheets and BP@PDA

The BP nanosheets were prepared from bulk BP crystals via ultrasonic exfoliation. Briefly, 10 mg of bulk BP was added to 50 ml of *N*-methyl pyrrolidone and sonicated in an ice bath for 24 hours at a low temperature. The resulting brown dispersion was then centrifuged at 2000 rpm for 10 min to remove the unexfoliated or thick-layered BP bulk. The BP nanosheets collected from the supernatant were washed with ethanol and ultrapure water via centrifugation at 13,000 rpm for 10 min to collect the sediment and for further modification. To synthesize the PDA-modified BP nanosheets (BP@PDA), the BP nanosheets were added to tris solution preadjusted to pH 8.5 using sodium hydroxide solution dissolved with dopamine hydrochloride and vigorously stirred for 2 hours. Then, the resulting dispersion was centrifuged (13,000 rpm for 10 min) and rinsed with ultrapure water to obtain the BP@PDA nanosheets.

Preparation of EA and EABP composite hydrogels

Pig subcutaneous fat was harvested from the market and processed under sterile conditions. Then, the tissue was treated with a decellularization process as previously reported with some modification (76). Briefly, the tissue was first freeze-thawed with three cycles (-80° to 37°C) in freezing buffer solution containing 10 mM tris and 5 mM EDTA. Next, the tissue was disrupted with a homogenizer, rinsed with PBS three times, further digested with enzymatic digestion solution consisting of 0.25% trypsin/0.02% EDTA (Beyotime, Shanghai, China), and incubated overnight at 37°C on a shaker bed at 1000 rpm. Subsequently, the tissue underwent 12 hours of polar solvent extraction using 99.9% isopropanol for the removal of the fatty liquid portion. After rinsing three times in PBS (pH 7.4), the tissue was incubated for 4 hours in the enzymatic digestion solution mentioned above. Following additional washes three times with PBS, the tissue was incubated in a solution containing 5000 U of deoxyribonuclease (Sigma-Aldrich), 10 mg of ribonuclease (Sigma-Aldrich), and 2000 U of lipase (Sigma-Aldrich) for 6 hours at 37°C . After rinsing three times in PBS, the tissue was treated in 99.9% isopropanol for 8 hours as a final polar solvent extraction. After washing the ECM three times using PBS, the ECM was fully disrupted with a homogenizer using 75% ethanol as the solvent. The resulting mixture was then vacuum-filtered to form a membrane, which was air-dried at room temperature (RT) and stored under vacuum for future use. The ECM membrane could be stored at 4°C for up to 6 months.

For gelation, the ECM membrane was digested in 0.5 M acetic acid at RT for 48 hours in constant rotation. The pregel was then centrifuged (300g for 10 min) to precipitate and eventually discard undigested particles. The remaining gelation was collected and freeze-dried after neutralizing to a physiological pH 7.4 by the addition of NaOH and thoroughly mixing according to a previous study with modification (77). AlgMA (EFL-Tech, China) was first incubated with 1-ethyl-3-[3-dimethylaminopropyl]carbodiimide (EDC; Aladdin Bio-Chem Technology, Shang Hai, China) and *N*-hydroxysulfosuccinimide (Sulfo-NHS; Aladdin Bio-Chem Technology, Shang Hai, China) to activate its carboxyl groups in MES buffer (pH 6.0). The resulting AlgMA with activated carboxyl groups was then dialyzed in distilled water using a dialysis bag (2000 Da; Spectrum, USA) for 3 days to remove the excess EDC or NHS. The resulting AlgMA was then freeze-dried, followed by mixing with ECM and dissolving in deionized water with 0.25% lithium phenyl-2,4,6-trimethylbenzoylphosphinate (EFL-Tech, China). After stirring for 1 hour at RT, the final concentration of the polymer was controlled at 2% (w/v), and the weight ratio of ECM and AlgMA was 1:1. The resulting composite hydrogel with or without BP@PDA nanosheets was then exposed to UV light (405 nm) for 20 s to light cure. The final composite hydrogels with low or high concentrations of BP@PDA were denoted EA (without BP@PDA nanosheets), EABP-100 (with 100 $\mu\text{g}/\text{ml}$ of BP@PDA nanosheets), and EABP-400 (with 400 $\mu\text{g}/\text{ml}$ of BP@PDA nanosheets).

Fabrication of the BD-ES system

To construct the closed-loop BD-ES system, the manufactured HTP-NG and EABP hydrogels were connected by copper wires in different ways. Before being used for biological verification, the BD-ES system was immersed in 75% ethanol solution for 30 min and exposed to UV radiation for 1 hour to achieve disinfection and sterilization.

Characterization and electrical measurement of the BD-ES system

A field-emission scanning electron microscope (Hitachi S-4800) was used to characterize the surface morphology of the PTFE film. The electrical properties of the EABP hydrogel were determined with an electrochemical workstation (CHI660E) in a standard three-electrode system with a conductive carbon fabric as the working electrode, an Ag/AgCl electrode as the reference electrode, and a Pt sheet as the counter electrode. A modal shaker (SA-JZ020) was used to provide the periodic external force applied to the HTP-NG to generate electric signals. The output performances of the HTP-NG were evaluated by a Keithley 6514 electrometer system (Keithley Instrument USA). A universal testing machine (HY-940FS), in conjunction with a software processing system (TM2101), was used to investigate the synergistic relationship between the applied force and output voltage of HTP-NG. In this test, the universal testing machine applied external pressure to the HTP-NG, while the commercial mechanical quantity sensor (BAB-20MT) was used to monitor the real-time force applied to the device.

Finite element analysis of BD-ES system based on COMSOL software

Finite element analysis of BD-ES system based on COMSOL software: The finite element calculation software COMSOL Multiphysics was used to simulate and estimate the output of BD-ES system. The model size refers to the actual size of the EABP hydrogel. The

voltage and electrical field change of the simulate electrode after being loaded are calculated. The material is EABP hydrogel. The load voltage was set at 0.8 V for the anode and ground for the cathode. The conductivity and relative permittivity are 0.12 S/m and 66.5, respectively.

Characterization of BP and BP@PDA

The samples were resuspended in deionized water before physicochemical property characterization. The diameter and zeta potential of the nanosheets were determined by DLS using a Nano instrument (Malvern Zetasizer Nano ZS90, UK). FTIR spectroscopy was performed via a Nicolet iS5 system (Thermo Fisher Scientific, USA). Raman spectra were obtained using Via Raman Microscope equipment (LabRAM HR800 Evolution, Horiba Scientific, France) with 532-nm laser excitation. TEM images were acquired by a Talos F200X (FEI, The Netherlands) microscope. The surface and height of the sample were detected by AFM using a Dimension ICON system (Bruker, USA).

Immunohistochemical analysis and DNA quantification of ECM

The native and decellularized tissue were fixed in 4% paraformaldehyde, followed by slicing after embedding in paraffin. Sections were then deparaffinized and dehydrated in ethanol. H&E staining and Masson's trichrome staining were first applied to detect the residual cells and the presence of collagen. Oil Red O staining was further used to assess the presence of lipids. In addition, the sections were stained with DAPI (Beyotime Biotechnology, Shanghai, China) at RT for 20 min to identify nucleic acids. The stained sections were observed using a fluorescence microscope (Leica, Germany). To further evaluate the efficiency of decellularization, the genomic DNA of native tissues and decellularized samples was extracted using a DNA Extraction kit (Tiangen Biotech, Beijing, China) according to the manufacturer's instructions, and then a NanoDrop2000 (Thermo Fisher Scientific, USA) was used to detect the concentration of DNA.

SEM of composite hydrogels

The hydrogel samples were washed with ultrapure water and lyophilized before SEM visualization (Hitachi Regulus8100, Japan).

In vitro swelling and degradation test

The swelling ratio was used to evaluate the substance exchange function of hydrogels. Lyophilized hydrogels were first weighed. Then, the hydrogel samples were immersed overnight in 3 ml of PBS (pH 7.4). Subsequently, the hydrogel samples were removed, and the free liquid was removed with filter paper. Then, the weight of the samples was recorded, and the swelling ratio was determined by the change in mass before and after as a percentage of dry weight. For the biodegradation test, the lyophilized hydrogel samples were immersed in 1 ml of PBS including collagenase I (2 U/ml). At a predetermined time, the remaining hydrogels were lyophilized, and their dried weight was measured. The degradation rate was assessed by calculating the percentage of the remaining weight after enzymatic degradation.

Rheological characteristics and lap shear test

Rheological characterization was performed by a rheometer (DHR, TA Instruments, USA). First, the hydrogel precursor was injected on the plate. After curing under UV light, a constant strain at a rate

of 1.0% and angular frequency at 10.0 rad/s was applied. Then, in the linear viscoelastic range of the system, a frequency sweep test was performed at a fixed strain of 1.0% and angular frequency of 10.0 rad/s. Last, the strain amplitude sweep test was conducted at a fixed angular frequency of 10.0 rad/s. The temperature of all the tests was set at 37°C. The adhesion properties of the composite hydrogels were determined by a universal machine tester (HY-940FS, Shanghai, China). For testing, the hydrogel was prepared with different concentrations as mentioned above. The samples for the test were attached between two glass slides. Pressure was applied at a rate of 5 mm/min to a maximal strain of 90%. The adhesion strength was determined by dividing the maximum load by the overlapping contact area.

Cell culture

BMSCs were obtained from the Cell Bank of the Chinese Academy of Sciences (Shanghai, China) and cultured in complete α -MEM with 10% fetal bovine serum (Gibco, USA) and 1% penicillin/streptomycin (Gibco, USA) in a humidified atmosphere of 5% CO₂ at 37°C. Hydrogel samples for cell experiments were exposed to UV light for 2 hours, sterilized with 75% ethanol for 30 min, and washed with PBS three times. To support osteogenic differentiation, the medium was replaced with complete α -MEM including L-ascorbic acid (50 μ g/ml; Sigma-Aldrich, USA), 10 mM β -glycerophosphate (Sigma-Aldrich, USA), and 10 nM dexamethasone (Sigma-Aldrich, USA) every 2 days.

External ES

Two parallel Pt rod electrodes connected with copper wire at the end were used to create electric fields in the assembled chamber. The hydrogel and the Pt rods were sterilized by exposure to UV light and 75% ethanol in the assembled chamber and washed with PBS three times for further use. BMSCs were then seeded into another plate and cultured for 6 hours to fully attach, followed by covering the hydrogels of each group. Then, these electrodes (15 mm) were inserted vertically into these hydrogels. By adjusting the frequency of the reciprocating motor and the distance between the reciprocating motor's force arm and the fixed HTP-NG, the output signals can be approximated to match the output parameters of HTP-NG during implantation within the body, and the electrical field was then applied across the two electrodes for 1 hour in the incubator daily to stimulate the cells. The electric field and current applied for stimulating BMSCs were uniformly controlled at \sim 0.5 V/mm and \sim 80 nA, respectively.

Cell biocompatibility and proliferation evaluations

The biocompatibility of the composite hydrogels was determined by a live/dead assay. Briefly, 1×10^5 BMSCs were seeded into 24-well plates for 6 hours to fully attach, followed by covering the hydrogels of each group, which were fully sterilized, and ensuring that the hydrogel could fully contact the cells. Then, the wells of the EA + ES group and EABP + ES group were stimulated via HTP-NG for 1 hour. After culturing for 24 hours, a live/dead assay kit (Beyotime, Shanghai, China) was used to assess the cell viability on the hydrogel using a fluorescence microscope (Leica DMI6000B, Germany). According to the above results, EABP-100 was selected for subsequent experiments. Unless otherwise indicated, EABP represents the EABP-100 composite hydrogel. To evaluate cell proliferation, BMSCs were seeded into 96-well plates for 6 hours to fully attach, and then they

were covered with EA and EABP hydrogels with or without ES. After 1, 3, 5, and 7 days, the hydrogels were removed gently, and a cell counting kit-8 (CCK-8; Beyotime, China) was applied to assess cell proliferation. Briefly, after removing the medium from the wells and washing three times with PBS, 100 μ l of serum-free medium and 10 μ l of CCK-8 solution were added to each well. After incubation at 37°C for 2 hours, absorbance at 450 nm was measured using a microplate reader (Thermo Fisher Scientific, USA).

Cell attachment and migration

To evaluate the migration ability of BMSCs under ES, EA or EABP-100 hydrogels were precured on the bottom of the culture plate. A total of 5.0×10^4 cells diluted in 200 μ l of serum-free medium were added to the upper chambers of a 24-well Transwell plate (3422, Corning, USA). Then, 500 μ l of complete medium was added to the lower chambers. After receiving ES for 1 hour and coculturing for another 12 hours, cells on the upper surface of the Transwell membrane were gently wiped with a cotton swab. Then, the Transwell inserts were washed with PBS and fixed with 4% paraformaldehyde for 15 min. Cells on the lower surface of the membrane were stained with 0.1% crystal violet for 10 min. Last, the Transwell inserts were washed with PBS to remove unbound crystal violet and air-dried. The migrated cells were observed and imaged under an inverted microscope (Leica, Germany). All the samples were assayed in triplicate, and each sample was observed with three random zones to count the migrated cells. To assess the spread morphology of BMSCs, BMSCs were seeded in 24-well plates covered with different hydrogels and cultured with absolute α -MEM medium with or without ES for 3 days. For fluorescence microscope observations, cells were rinsed with PBS and fixed in 4% formaldehyde solution for 15 min. After washing three times with PBS, the cells were incubated with anti-vinculin-FITC antibody for 1 hour, followed by staining with rhodamine-phalloidin for 45 min and incubation with DAPI for 5 min. Fluorescence images were taken on a fluorescence microscope (Leica, Germany).

Measurement of intracellular calcium levels

Intracellular calcium levels were measured with Fluo-4 direct calcium assay kits (Beyotime, China). After 1 hour of ES, the culture medium was removed from the wells and washed with PBS three times, followed by the addition of 100 μ l of the Fluo-4 direct calcium reagent and incubation at 37°C for 10 min. Then, the stained cells were observed using a fluorescence microscope, and the mean fluorescence intensity was analyzed via ImageJ software. Similarly, cells in another cell culture plate covered with EABP received ES for 20, 40, and 60 min, followed by staining with Fluo-4 direct calcium reagent as described above. These stained cells were collected and washed with PBS after digestion with trypsin without EDTA. Last, the cells in each well were diluted with PBS and measured by flow cytometry at 488 nm.

Alkaline phosphatase staining

After being treated with or without ES for 7 and 14 days in osteogenic medium, BMSCs were stained with a bromochloroindolyl phosphate-nitro blue tetrazolium (BCIP/NBT) alkaline phosphatase staining kit (Beyotime, Beijing, China). Briefly, cells in each well were washed with PBS and fixed with 4% paraformaldehyde for 15 min. After washing with PBS three times, BCIP/NBT solution was added to each well and incubated for 30 min at RT. Then, the cells in

each well were rinsed with PBS three times and observed under a microscope. Subsequently, quantification of the stained area was calculated using ImageJ to evaluate the ALP level.

Alizarin red staining

BMSCs were treated with or without ES for 21 days in osteogenic medium, and the formation of mineralized matrix nodules was observed using the Alizarin Red S Staining Kit following the manufacturers' instructions. Briefly, cells in each well were washed with PBS and fixed with 4% paraformaldehyde for 15 min. After washing with deionized water three times, alizarin red S reagent was added to each well and incubated for 30 min at RT. Then, the cells in each well were rinsed with deionized water three times and observed under a microscope. The average integrated optical density was analyzed by ImageJ.

Western blot

For Western blotting, BMSCs were lysed with radioimmunoprecipitation assay lysis buffer containing phosphatase and protease inhibitors (Thermo Fisher Scientific, USA) for 30 min on ice and cleared by centrifugation at 12,000g for 30 min at 4°C. The total protein concentration of the cell lysates was determined using a Pierce BCA Protein Assay Kit (Thermo Fisher Scientific, USA). Ten micrograms of each sample was mixed with 5 \times SDS loading buffer and denatured at 100°C for 5 min. The reduced samples were loaded and separated by 10% or 6% SDS-polyacrylamide gel electrophoresis and transferred to nitrocellulose (NC) membranes (Bio-Rad) after separation. The membrane was then blocked in 5% bovine serum albumin (BSA) in blocking buffer of Tris buffered saline with Tween-20 (TBS-T) for 2 hours at RT and incubated with antibodies specific for OCN (Abcam, UK), Ocn (Abcam, UK), OPN (Abcam, UK), RUNX2 (Abcam, UK), PI3K (Invitrogen, USA), p-PI3K (Invitrogen, USA), AKT (Invitrogen, USA), p-AKT (Invitrogen, USA), PIEZO1 (Invitrogen, USA), PIEZO2 (Invitrogen, USA), WNT11 (Abcam, UK), RAS (Abcam, UK), ERK1/2 (Invitrogen, USA), p-ERK1/2 (Invitrogen, USA), and glyceraldehyde-3-phosphate dehydrogenase (GAPDH; Abcam, UK) following the manufacturer's instructions in blocking buffer overnight at 4°C. The membranes were then rinsed with TBS-T, and secondary antibodies were applied in TBS-T for 2 hours. The secondary antibody rabbit-horse radish peroxidase (Santa Cruz Biotechnology) was used at a 1:3000 dilution with TBS-T and incubated for 2 hours at RT. After washing with TBS-T, protein signals were visualized using SuperSignal West Pico PLUS Chemiluminescent Substrate (34,579; Thermo Fisher Scientific) and captured by a Tanon 5200 imaging system (Shanghai Tennant Life Science Co.).

Transcriptome sequencing and data analysis

BMSCs (5×10^6 cells/ml) were stimulated with the BD-ES system as described above for 7 days and cultured in osteogenic medium. Cells in the control group did not receive stimulation. Cells in the two groups were then lysed using TRIzol reagent (Ambion, Carlsbad, CA), and cell lysates were stored at -80°C before sequencing. RNA-seq was performed by Illumina HiSeq X10 (Illumina, USA). Genefund Biotech (Shanghai, China) conducted the quality control, comparison, and quantification of raw RNA-seq data to assess expression levels. RNA-seq expression data analysis was conducted using R (version 4.2.3). The limma package (78) was used to normalize gene expression levels and detect DEGs, applying a minimum

1.5-fold change and a *P* value cutoff of less than 0.05 as filtering criteria. The clusterProfiler package (79) was used to perform functional enrichment analysis of the identified DEGs.

qPCR assay

BMSCs were cultured in accordance with the previously described protocol. Briefly, a total of 2×10^5 cells per well were seeded into six-well plates. Following cell adhesion to the surface, the culture medium was replaced and supplemented with 10 mM β -glycerophosphate, L-ascorbic acid phosphate (50 μ g/ml), and 10 nM dexamethasone. BD-ES system was subsequently used to stimulate the cells as described above for 7 days, and tissue culture plastic served as a control. Subsequently, the expression levels of osteogenic-related genes, including *OCN*, *OPN*, and *RUNX2*, were assessed by real-time PCR. Total RNA was extracted from BMSCs using Total RNA Extraction Reagent (TRIzol, Invitrogen, USA) following the manufacturer's instructions. After reverse transcription using PrimeScript RT reagent (Takara, China), the total RNA was quantified through quantitative PCR (qPCR). These levels were then expressed as relative values, normalized to the gene expression of GAPDH mRNA. The primer sequences used for this analysis are provided in table S6.

Biocompatibility evaluation of the BD-ES system in vivo

All animal experiments were carried out according to protocols approved by the Animal Care and Use Committee of Shanghai Tenth People's Hospital, School of Medicine, Tongji University, Shanghai, China (ethical approval number: SHDSYY-2022-2530). The biocompatibility of EA and EABP hydrogels was first evaluated in vitro using a hemolysis test. Blood was taken from male Sprague-Dawley rats and washed three times by centrifugation with 0.9% normal saline. The precipitate was then diluted with 0.9% saline into a 0.2% (v/v) red blood cell suspension. Deionized water was used as the positive control group, and 0.9% saline was used as the negative control group. An equal volume of red blood cell suspension was incubated with hydrogel (5 mm in diameter, 3 mm in height). After incubation at 37°C for 4 hours, the supernatant of each group was harvested by centrifugation at 1500 rpm for 15 min, and the absorbance was measured at 541 nm. The hemolysis rate of each group was calculated according to the following equation: Hemolysis rate = (Absorbance of the sample) – (Absorbance of negative control)/(Absorbance of positive control) – (Absorbance of negative control). To evaluate the biocompatibility of EA and EABP hydrogels in vivo, male Sprague-Dawley rats were randomly assigned into two groups with two animals per group. Each pentobarbital-anesthetized rat had three preformed gels (5 mm in diameter, 3 mm in height) subcutaneously implanted in the back. The rats were sacrificed at 2 weeks, and the gels in vivo and surrounding tissue were fixed in paraformaldehyde solution for further immunohistochemical staining, including H&E and IL-6 staining. The biocompatibility of the triboelectric nanogenerator (TEG) was assessed by histological assessment of H&E staining. After subcutaneous implantation in front of the knee for 2 weeks, the subcutaneous tissue was harvested to assess the biocompatibility of the TENG. All the samples were dehydrated, embedded in paraffin, and sliced for histological staining. Images were obtained via an immunofluorescence microscope (Leica, Germany).

Implantation of the BD-ES system and in vivo regeneration of femoral critical-size BDs

For BD-ES system implantation in vivo, male Sprague-Dawley rats (12 weeks) were used as the standard animal models. Before the implantation of the BD-ES system, the HTP-NGs were sterilized by UV for 4 hours. Rats were first anesthetized using sodium pentobarbital via intraperitoneal injection. The surgical region was then shaved and cleaned with povidone/iodine solution. The skin was incised longitudinally along the right femur, and a cylindrical defect with a 3-mm diameter was formed at the right femoral condyles. For the ES+ group, a small incision was created longitudinally along the right knee, followed by placing the HTP-NG subcutaneously, which was fixed in front of the knee to sense the deformation caused by knee joint activities. The proximal end of the HTP-NG is connected with a Pt soft wire. Then, the distal end of the Pt soft wire crossed from the subcutaneous abdomen to the femoral defect, and the distal end of the wire was embedded via the injection and further curing of the hydrogel under UV light. After successful construction of the BD-ES system in vivo, the incision was fully sterilized and sutured. In addition, 3D-reconstructed CT was performed to confirm that there was no displacement of the HTP-NG at 2 weeks after surgery. All rats ran at a speed of 1 km/hour for 30 min daily on a homemade track and rested for 2 min every 5 min. The output voltage of the HTP-NG was driven and recorded using a Keithley 6514 electrometer system in the running state. Furthermore, rats in other groups were also asked to exercise as described above to evaluate the effect of ES on bone repair in the context of rehabilitation. After exercise for another 4 weeks, a CT scan was performed to assess the position of the HTP-NG, and the femur with the defect was harvested and fixed in 4.0% paraformaldehyde at 4°C for further use.

Micro-computed tomography

To evaluate the effect on bone regeneration, the femurs were scanned and analyzed using a micro-CT system at 10- μ m resolution (Sky-Scan 1276, Bruker, Belgium). The cylindrical BD region (diameter: 3 mm and depth: 4 mm) was set as the region of interest for quantitative analysis of typical parameters. Trabecular bone parameters were measured, including BMD (g/cm^3), BV/TV (%), Tb.N (1/mm), and Tb.Th (mm).

Histology and immunohistochemistry

After decalcification following the micro-CT scan, the samples were dehydrated in a graded ethanol series and embedded in paraffin. Then, sections of approximately 5 μ m were obtained for further staining. First, H&E and Masson's trichrome staining were performed to evaluate bone formation and residual materials. In addition, some deparaffinized sections were subjected to IL-6 and TNF- α staining to evaluate the levels of inflammatory cytokines. Furthermore, immunofluorescence staining was carried out to evaluate the expression of osteogenic marker proteins, including OCN and OPN. The microvessel density (MVD) was also evaluated by CD31/ α -SMA immunofluorescence staining. The quantification of MVD was determined by averaging the number of positive cells in three vascularized regions. Briefly, the deparaffinized sections were first blocked with 5% BSA solution, followed by incubation with primary antibodies against OCN, OPN, and RUNX2 or angiogenesis markers of CD31/ α -SMA at a 1:100 dilution overnight at 4°C. In addition, to assess the potential toxicity of implanted scaffolds in vivo, major organs, including the heart, liver, spleen, lung, and kidney,

were collected at 6 weeks and stained with H&E. All samples were imaged with an optical microscope.

Statistical analysis

All data collected in this work are expressed as means \pm SD and were analyzed with SPSS (IBM SPSS Statistics for Windows, version 25.0). One-way analysis of variance (ANOVA) or two-way ANOVA with Tukey's multiple comparisons test was performed to identify significant differences between groups. To compare the means of two independent groups, an unpaired Student's *t* test was performed. Differences were considered significant at $*P < 0.05$ and $**P < 0.01$ or were considered highly significant at $***P < 0.001$.

Supplementary Materials

This PDF file includes:

Figs. S1 to S41

Tables S1 to S6

Legends for movies S1 to S3

Other Supplementary Material for this manuscript includes the following:

Movies S1 to S3

REFERENCES AND NOTES

- W. Wang, K. W. K. Yeung, Bone grafts and biomaterials substitutes for bone defect repair: A review. *Bioact. Mater.* **2**, 224–247 (2017).
- S. Singh, E. L. Nyberg, A. N. O'Sullivan, A. Farris, A. N. Rindone, N. Zhang, E. C. Whitehead, Y. Zhou, E. Mihaly, C. C. Acchebe, W. Zbijewski, W. Grundy, D. Garlick, N. D. Jackson, T. Taguchi, C. Takawira, J. Lopez, M. J. Lopez, M. P. Grant, W. L. Grayson, Point-of-care treatment of geometrically complex midfacial critical-sized bone defects with 3D-printed scaffolds and autologous stromal vascular fraction. *Biomaterials* **282**, 121392 (2022).
- K. Liu, L. Li, J. Chen, Y. Li, W. Wen, L. Lu, L. Li, H. Li, M. Liu, C. Zhou, B. Luo, Bone ECM-like 3D printing scaffold with liquid crystalline and viscoelastic microenvironment for bone regeneration. *ACS Nano* **16**, 21020–21035 (2022).
- Y. Ha, X. Ma, S. Li, T. Li, Z. Li, Y. Qian, M. Shafiq, J. Wang, X. Zhou, C. He, Bone microenvironment-mimetic scaffolds with hierarchical microstructure for enhanced vascularization and bone regeneration. *Adv. Funct. Mater.* **32**, 2200011 (2022).
- G. Hendrickx, V. Fischer, A. Liedert, S. von Kroge, M. Haffner-Luntzer, L. Brylka, E. Pawlus, M. Schweizer, T. Yorgan, A. Baranowsky, T. Rolvien, M. Neven, U. Schumacher, D. J. Beech, M. Amling, A. Ignatius, T. Schinke, Piezo1 inactivation in chondrocytes impairs trabecular bone formation. *J. Bone Miner. Res.* **36**, 369–384 (2021).
- Y. Wan, H. Wang, X. Fan, J. Bao, S. Wu, Q. Liu, X. Yan, J. Zhang, Z. B. Jin, B. Xiao, N. Wang, Mechanosensitive channel Piezo1 is an essential regulator in cell cycle progression of optic nerve head astrocytes. *Glia* **71**, 1233–1246 (2023).
- L. Wang, X. You, L. Zhang, C. Zhang, W. Zou, Mechanical regulation of bone remodeling. *Bone Res.* **10**, 16 (2022).
- S. Onuora, Electric scaffolds charge cartilage repair. *Nat. Rev. Rheumatol.* **18**, 127 (2022).
- Y. Liu, G. Dzditor, T. T. Le, T. Vinikoor, K. Morgan, E. J. Curry, R. Das, A. McClinton, E. Eisenberg, L. N. Apuzzo, K. T. M. Tran, P. Prasad, T. J. Flanagan, S.-W. Lee, H.-M. Kan, M. T. Chorsi, K. W. H. Lo, C. T. Laurencin, T. D. Nguyen, Exercise-induced piezoelectric stimulation for cartilage regeneration in rabbits. *Sci. Transl. Med.* **14**, eabi7282 (2022).
- A. Goel, M. Leong, H. J. J. Shanthanna, Spinal cord burst stimulation vs placebo stimulation for patients with chronic radicular pain after lumbar spine surgery. *JAMA* **329**, 846–847 (2023).
- G. Yao, L. Kang, C. Li, S. Chen, Q. Wang, J. Yang, Y. Long, J. Li, K. Zhao, W. Xu, W. Cai, Y. Lin, X. Wang, A self-powered implantable and bioresorbable electrostimulation device for biofeedback bone fracture healing. *Proc. Natl. Acad. Sci. U.S.A.* **118**, e2100772118 (2021).
- X. Peng, K. Dong, C. Ye, Y. Jiang, S. Zhai, R. Cheng, D. Liu, X. Gao, J. Wang, Z. L. Wang, A breathable, biodegradable, antibacterial, and self-powered electronic skin based on all-nanofiber triboelectric nanogenerators. *Sci. Adv.* **6**, eaba9624 (2020).
- F.-R. Fan, Z.-Q. Tian, Z. L. Wang, Flexible triboelectric generator. *Nano Energy* **1**, 328–334 (2012).
- C. Chen, S. Zhao, C. Pan, Y. Zi, F. Wang, C. Yang, Z. L. Wang, A method for quantitatively separating the piezoelectric component from the as-received "piezoelectric" signal. *Nat. Commun.* **13**, 1391 (2022).
- J. Yu, X. Hou, M. Cui, S. Zhang, J. He, W. Geng, J. Mu, X. Chou, Highly skin-conformal wearable tactile sensor based on piezoelectric-enhanced triboelectric nanogenerator. *Nano Energy* **64**, 103923 (2019).
- W.-T. Cao, H. Ouyang, W. Xin, S. Chao, C. Ma, Z. Li, F. Chen, M.-G. Ma, A stretchable highoutput triboelectric nanogenerator improved by MXene liquid electrode with high electronegativity. *Adv. Funct. Mater.* **30**, 2004181 (2020).
- Z. Deng, L. Xu, H. Qin, X. Li, J. Duan, B. Hou, Z. L. Wang, Rationally structured triboelectric nanogenerator arrays for harvesting water-current energy and self-powered sensing. *Adv. Mater.* **34**, e2205064 (2022).
- M. Mariello, L. Fachechi, F. Guido, M. De Vittorio, Conformal, ultra-thin skin-contact-actuated hybrid piezo/triboelectric wearable sensor based on AlN and parylene-encapsulated elastomeric blend. *Adv. Funct. Mater.* **31**, 2101047 (2021).
- M. Zhu, M. Lou, J. Yu, Z. Li, B. Ding, Energy autonomous hybrid electronic skin with multi-modal sensing capabilities. *Nano Energy* **78**, 105208 (2020).
- Z. Wang, X. Liu, M. Yue, H. Yao, H. Tian, X. Sun, Y. Wu, Z. Huang, D. Ban, H. Zheng, Hybridized energy harvesting device based on high-performance triboelectric nanogenerator for smart agriculture applications. *Nano Energy* **102**, 107681 (2022).
- D. Tan, Q. Zeng, X. Wang, S. Yuan, Y. Luo, X. Zhang, L. Tan, C. Hu, G. Liu, Anti-overturning fully symmetrical triboelectric nanogenerator based on an elliptical cylindrical structure for all-weather blue energy harvesting. *Nanomicro Lett.* **14**, 124 (2022).
- S. Yao, X. Zhao, X. Wang, T. Huang, Y. Ding, J. Zhang, Z. Zhang, Z. L. Wang, L. Li, Bioinspired electron polarization of nanozymes with a human self-generated electric field for cancer catalytic therapy. *Adv. Mater.* **34**, e2109568 (2022).
- X. Qu, Z. Liu, P. Tan, C. Wang, Y. Liu, H. Feng, D. Luo, Z. Li, Z. L. Wang, Artificial tactile perception smart finger for material identification based on triboelectric sensing. *Sci. Adv.* **8**, eabq2521 (2022).
- Q. Zheng, Q. Tang, Z. L. Wang, Z. Li, Self-powered cardiovascular electronic devices and systems. *Nat. Rev. Cardiol.* **18**, 7–21 (2021).
- P. Tan, X. Han, Y. Zou, X. Qu, J. Xue, T. Li, Y. Wang, R. Luo, X. Cui, Y. Xi, L. Wu, B. Xue, D. Luo, Y. Fan, X. Chen, Z. Li, Z. L. Wang, Self-powered gesture recognition wristband enabled by machine learning for full keyboard and multicommand input. *Adv. Mater.* **34**, e2200793 (2022).
- J. Zheng, Z. Yu, Y. Wang, Y. Fu, D. Chen, H. Zhou, Acoustic core-shell resonance harvester for application of artificial cochlea based on the piezo-triboelectric effect. *ACS Nano* **15**, 17499–17507 (2021).
- G. Conta, A. Libanori, T. Tat, G. Chen, J. Chen, Triboelectric nanogenerators for therapeutic electrical stimulation. *Adv. Mater.* **33**, e2007502 (2021).
- Z.-Y. Huo, Y.-J. Kim, I.-Y. Suh, D.-M. Lee, J. H. Lee, Y. Du, S. Wang, H.-J. Yoon, S.-W. Kim, Triboelectricity induced self-powered microbial disinfection using nanowire-enhanced localized electric field. *Nat. Commun.* **12**, 3693 (2021).
- F. Jin, T. Li, T. Yuan, L. Du, C. Lai, Q. Wu, Y. Zhao, F. Sun, L. Gu, T. Wang, Z.-Q. Feng, Physiologically self-regulated, fully implantable, battery-free system for peripheral nerve restoration. *Adv. Mater.* **33**, e2104175 (2021).
- Y. Sun, S. Chao, H. Ouyang, W. Zhang, W. Luo, Q. Nie, J. Wang, C. Luo, G. Ni, L. Zhang, J. Yang, H. Feng, G. Mao, Z. Li, Hybrid nanogenerator based closed-loop self-powered low-level vagus nerve stimulation system for atrial fibrillation treatment. *Sci. Bull.* **67**, 1284–1294 (2022).
- Y. Long, J. Li, F. Yang, J. Wang, X. Wang, Wearable and implantable electroceuticals for therapeutic electrostimulations. *Adv. Sci.* **8**, 2004023 (2021).
- J. Tian, R. Shi, Z. Liu, H. Ouyang, M. Yu, C. Zhao, Y. Zou, D. Jiang, J. Zhang, Z. Li, Self-powered implantable electrical stimulator for osteoblasts' proliferation and differentiation. *Nano Energy* **59**, 705–714 (2019).
- C. D. McCaig, M. Zhao, Physiological electrical fields modify cell behaviour. *Bioessays* **19**, 819–826 (1997).
- L. Tong, Q. Liao, Y. Zhao, H. Huang, A. Gao, W. Zhang, X. Gao, W. Wei, M. Guan, P. K. Chu, H. Wang, Near-infrared light control of bone regeneration with biodegradable photothermal osteoimplant. *Biomaterials* **193**, 1–11 (2019).
- A. Bashiri Rezaie, M. Liebscher, M. Ranjbarian, F. Simon, C. Zimmerer, A. Drechsler, R. Frenzel, A. Synytska, V. Mechtcherine, Enhancing the interfacial bonding between PE fibers and cementitious matrices through polydopamine surface modification. *Compos. B Eng.* **217**, 108817 (2021).
- C. M. Said, M. Delahunt, A. Hardidge, P. Smith, P. Tran, L. McDonald, E. Kefalianos, C. Daniel, S. Berney, Recumbent cycling to improve outcomes in people with hip fracture: A feasibility randomized trial. *BMC Geriatr.* **21**, 394 (2021).
- N. Simunovic, P. J. Devereaux, S. Sprague, G. H. Guyatt, E. Schemitsch, J. Debeer, M. Bhandari, Effect of early surgery after hip fracture on mortality and complications: Systematic review and meta-analysis. *CMAJ* **182**, 1609–1616 (2010).
- J. Magaziner, K. Mangione, D. Orwig, M. Baumgarten, L. Magder, M. Terrin, R. Fortinsky, A. Gruber-Baldini, B. Beamer, A. Tosteson, A. Kenny, M. Shardell, E. Binder, K. Koval, B. Resnick, R. Miller, S. Forman, R. McBride, R. J. J. Craik, Effect of a multicomponent home-based physical therapy intervention on ambulation after hip fracture in older adults: The cap randomized clinical trial. *JAMA* **322**, 946–956 (2019).
- L. Cui, J. Zhang, J. Zou, X. Yang, H. Guo, H. Tian, P. Zhang, Y. Wang, N. Zhang, X. Zhuang, Z. Li, J. Ding, X. Chen, Electroactive composite scaffold with locally expressed osteoinductive factor for synergistic bone repair upon electrical stimulation. *Biomaterials* **230**, 119617 (2020).

40. J. Mi, J.-K. Xu, Z. Yao, H. Yao, Y. Li, X. He, B.-Y. Dai, L. Zou, W.-X. Tong, X.-T. Zhang, P.-J. Hu, Y. C. Ruan, N. Tang, X. Guo, J. Zhao, J.-F. He, L. Qin, Implantable electrical stimulation at dorsal root ganglions accelerates osteoporotic fracture healing via calcitonin gene-related peptide. *Adv. Sci.* **9**, e2103005 (2022).
41. Z. Wen, M.-H. Yeh, H. Guo, J. Wang, Y. Zi, W. Xu, J. Deng, L. Zhu, X. Wang, C. Hu, L. Zhu, X. Sun, Z. L. Wang, Self-powered textile for wearable electronics by hybridizing fiber-shaped nanogenerators, solar cells, and supercapacitors. *Sci. Adv.* **2**, e1600097 (2016).
42. P. Zhu, Y. Wang, Y. Wang, H. Mao, Q. Zhang, Y. Deng, Flexible 3D architected piezo/thermoelectric bimodal tactile sensor array for E-skin application. *Adv. Energy Mater.* **10**, 2001945 (2020).
43. B. Seo, Y. Cha, S. Kim, W. Choi, Rational design for optimizing hybrid thermo-triboelectric generators targeting human activities. *ACS Energy Lett.* **4**, 2069–2074 (2019).
44. Z. Shen, S.-T. Sun, W. Wang, J. Liu, Z. Liu, J. C. Yu, A black–red phosphorus heterostructure for efficient visible-light-driven photocatalysis. *J. Mater. Chem. A* **3**, 3285–3288 (2015).
45. C. Xu, Y. Xu, M. Yang, Y. K. Chang, A. M. Nie, Z. Y. Liu, J. L. Wang, Z. Q. Luo, Black-phosphorus-incorporated hydrogel as a conductive and biodegradable platform for enhancement of the neural differentiation of mesenchymal stem cells. *Adv. Funct. Mater.* **30**, 2000177 (2020).
46. W. Cheng, J. Nie, L. Xu, C. Liang, Y. Peng, G. Liu, T. Wang, L. Mei, L. Huang, X. Zeng, pH-sensitive delivery vehicle based on folic acid-conjugated polydopamine-modified mesoporous silica nanoparticles for targeted cancer therapy. *ACS Appl. Mater. Interfaces* **9**, 18462–18473 (2017).
47. D. A. Young, Y. S. Choi, A. J. Engler, K. L. Christman, Stimulation of adipogenesis of adult adipose-derived stem cells using substrates that mimic the stiffness of adipose tissue. *Biomaterials* **34**, 8581–8588 (2013).
48. H. L. Xu, J. Xu, S. S. Zhang, Q. Y. Zhu, B. H. Jin, D. L. ZhuGe, B. X. Shen, X. Q. Wu, J. Xiao, Y. Z. Zhao, Temperature-sensitive heparin-modified poloxamer hydrogel with affinity to KGF facilitate the morphologic and functional recovery of the injured rat uterus. *Drug Deliv.* **24**, 867–881 (2017).
49. Y. N. Chen, G. L. Cui, N. H. Dan, Y. P. Huang, Z. X. Bai, C. K. Yang, W. H. Dan, Preparation and characterization of dopamine-sodium carboxymethyl cellulose hydrogel. *SN Appl. Sci.* **1**, 609 (2019).
50. X. Yang, E. Bakaic, T. Hoare, E. D. Cranston, Injectable polysaccharide hydrogels reinforced with cellulose nanocrystals: Morphology, rheology, degradation, and cytotoxicity. *Biomacromolecules* **14**, 4447–4455 (2013).
51. H. Liu, C. Li, B. Wang, X. Sui, L. Wang, X. Yan, H. Xu, L. Zhang, Y. Zhong, Z. Mao, Self-healing and injectable polysaccharide hydrogels with tunable mechanical properties. *Cellulose* **25**, 559–571 (2018).
52. H. Mokhtari, M. Kharaziha, F. Karimzadeh, S. Tavakoli, An injectable mechanically robust hydrogel of κ -carrageenan-dopamine functionalized graphene oxide for promoting cell growth. *Carbohydr. Polym.* **214**, 234–249 (2019).
53. H. Lee, S. M. Dellatore, W. M. Miller, P. B. Messersmith, Mussel-inspired surface chemistry for multifunctional coatings. *Science* **318**, 426–430 (2007).
54. Y. Watanabe, T. Nakayama, D. Nagakubo, K. Hieshima, Z. Jin, F. Katou, K. Hashimoto, O. Yoshie, Dopamine selectively induces migration and homing of naive CD8⁺ T cells via dopamine receptor D3. *J. Immunol.* **176**, 848–856 (2006).
55. R. Babona-Pilipos, N. Liu, A. Pritchard-Oh, A. Mok, D. Badawi, M. R. Popovic, C. M. Morshead, Calcium influx differentially regulates migration velocity and directedness in response to electric field application. *Exp. Cell Res.* **368**, 202–214 (2018).
56. G. Murillo, A. Blanquer, C. Vargas-Estevez, L. Barrios, E. Ibáñez, C. Nogués, J. Esteve, Electromechanical nanogenerator–cell interaction modulates cell activity. *Adv. Mater.* **29**, 1605048 (2017).
57. X. Chen, W. Pan, Y. Sui, H. Li, X. Shi, X. Guo, H. Qi, C. Xu, W. Liu, Acidic phospholipids govern the enhanced activation of IgG-B cell receptor. *Nat. Commun.* **6**, 8552 (2015).
58. J. Wu, Q. Zhao, G. Wu, H. Yuan, Y. Ma, H. Lin, L. Pan, S. Li, D. Sun, Comprehensive analysis of differentially expressed unigenes under NaCl stress in flax (*Linum usitatissimum* L.) using RNA-seq. *Int. J. Mol. Sci.* **20**, 369 (2019).
59. J. Li, H. Du, X. Ji, Y. Chen, Y. Li, B. C. Heng, J. Xu, ETV2 promotes osteogenic differentiation of human dental pulp stem cells through the ERK/MAPK and PI3K-Akt signaling pathways. *Stem Cell. Res. Ther.* **13**, 495 (2022).
60. H. Cui, G. Han, B. Sun, X. Fang, X. Dai, S. Zhou, H. Mao, B. Wang, Activating PIK3CA mutation promotes osteogenesis of bone marrow mesenchymal stem cells in macrodactyly. *Cell Death Dis.* **11**, 505 (2020).
61. M. M. Dvorak, D. Riccardi, Ca²⁺ as an extracellular signal in bone. *Cell Calcium* **35**, 249–255 (2004).
62. S. Du, H. Suo, G. Xie, Q. Lyu, M. Mo, Z. Xie, N. Zhou, L. Zhang, J. Tao, J. Zhu, Self-powered and photothermal electronic skin patches for accelerating wound healing. *Nano Energy* **93**, 106906 (2022).
63. S.-H. Jeong, Y. Lee, M.-G. Lee, W. J. Song, J.-U. Park, J.-Y. Sun, Accelerated wound healing with an ionic patch assisted by a triboelectric nanogenerator. *Nano Energy* **79**, 105463 (2021).
64. S. Lee, H. Wang, Q. Shi, L. Dhakar, J. Wang, N. V. Thakor, S.-C. Yen, C. Lee, Development of battery-free neural interface and modulated control of tibialis anterior muscle via common peroneal nerve based on triboelectric nanogenerators (TENGS). *Nano Energy* **33**, 1–11 (2017).
65. G.-T. Hwang, Y. Kim, J.-H. Lee, S. Oh, C. K. Jeong, D. Y. Park, J. Ryu, H. Kwon, S.-G. Lee, B. Joung, D. Kim, K. J. Lee, Self-powered deep brain stimulation via a flexible PIMNT energy harvester. *Energ. Environ. Sci.* **8**, 2677–2684 (2015).
66. P. Chen, P. Wu, X. Wan, Q. Wang, C. Xu, M. Yang, J. Feng, B. Hu, Z. Luo, Ultrasound-driven electrical stimulation of peripheral nerves based on implantable piezoelectric thin film nanogenerators. *Nano Energy* **86**, 106123 (2021).
67. M. Zhou, M. Huang, H. Zhong, C. Xing, Y. An, R. Zhu, Z. Jia, H. Qu, S. Zhu, S. Liu, L. Wang, H. Ma, Z. Qu, G. Ning, S. Feng, Contact separation triboelectric nanogenerator based neural interfacing for effective sciatic nerve restoration. *Adv. Funct. Mater.* **32**, 2200269 (2022).
68. Q. Zheng, B. Shi, F. Fan, X. Wang, L. Yan, W. Yuan, S. Wang, H. Liu, Z. Li, Z. L. Wang, In vivo powering of pacemaker by breathing-driven implanted triboelectric nanogenerator. *Adv. Mater.* **26**, 5851–5856 (2014).
69. H. Ouyang, Z. Liu, N. Li, B. Shi, Y. Zou, F. Xie, Y. Ma, Z. Li, H. Li, Q. Zheng, X. Qu, Y. Fan, Z. L. Wang, H. Zhang, Z. Li, Symbiotic cardiac pacemaker. *Nat. Commun.* **10**, 1821 (2019).
70. M. Marenzana, T. R. Arnett, The key role of the blood supply to bone. *Bone Res.* **1**, 203–215 (2013).
71. S. B. Lang, Pyroelectric effect in bone and tendon. *Nature* **212**, 704–705 (1966).
72. C. A. Bassett, S. N. Mitchell, S. R. Gaston, Treatment of ununited tibial diaphyseal fractures with pulsing electromagnetic fields. *J. Bone Joint Surg. Am.* **63**, 511–523 (1981).
73. D. M. Lee, M. Kang, I. Hyun, B. J. Park, H. J. Kim, S. H. Nam, H. J. Yoon, H. Ryu, H. M. Park, B. O. Choi, S. W. Kim, An on-demand bioresorbable neurostimulator. *Nat. Commun.* **14**, 7315 (2023).
74. F. Yang, J. Li, Y. Long, Z. Zhang, L. Wang, J. Sui, Y. Dong, Y. Wang, R. Taylor, D. Ni, W. Cai, P. Wang, T. Hacker, X. Wang, Wafer-scale heterostructured piezoelectric bio-organic thin films. *Science* **373**, 337–342 (2021).
75. J. Li, Y. Long, F. Yang, X. Wang, Degradable piezoelectric biomaterials for wearable and implantable bioelectronics. *Curr. Opin. Solid State Mater. Sci.* **24**, 100806 (2020).
76. L. E. Flynn, The use of decellularized adipose tissue to provide an inductive microenvironment for the adipogenic differentiation of human adipose-derived stem cells. *Biomaterials* **31**, 4715–4724 (2010).
77. G. G. Giobbe, C. Crowley, C. Luni, S. Campinoti, M. Khedr, K. Kretzschmar, M. M. De Santis, E. Zambaiti, F. Michielin, L. Meran, Q. Hu, G. van Son, L. Urbani, A. Manfredi, M. Giomo, S. Eaton, D. Cacchiarelli, V. S. W. Li, H. Clevers, P. Bonfanti, N. Elvassore, P. De Coppi, Extracellular matrix hydrogel derived from decellularized tissues enables endodermal organoid culture. *Nat. Commun.* **10**, 5658 (2019).
78. M. E. Ritchie, B. Phipson, D. Wu, Y. Hu, C. W. Law, W. Shi, G. K. Smyth, limma powers differential expression analyses for RNA-sequencing and microarray studies. *Nucleic Acids Res.* **43**, e47 (2015).
79. T. Wu, E. Hu, S. Xu, M. Chen, P. Guo, Z. Dai, T. Feng, L. Zhou, W. Tang, L. Zhan, X. Fu, S. Liu, X. Bo, G. Yu, clusterProfiler 4.0: A universal enrichment tool for interpreting omics data. *Innovation* **2**, 100141 (2021).

Acknowledgments

Funding: This work was supported by National Key R&D Program of China grants 2022YFC2504304 (to L. Zheng) and 2022YFE0123500 (to F.C.); National Natural Science Foundation of China grants 82372395 (to L. Zheng), T2125003 (to Z. Li), 62004010 (to H.O.), and 52202108 (to W.C.); Science and Technology Commission of Shanghai Municipality grants 23S31905700 (to L. Zheng) and 22S31903300 (to F.C.); Youth Innovation Promotion Association CAS grant 2023176 (to H.O.); The Fundamental Research Funds for the Central Universities E0EG6802X2 (to Z. Li) and 22120210582 (to W.C.); Beijing Natural Science Foundation grants JQ20038 (to Z. Li), L212010 (to Z. Li), and 7232347 (to H.O.); and China Postdoctoral Science Foundation 2021TQ0247 (to W.C.) and 2022 M712395 (to W.C.). **Author contributions:** Conceptualization: T.W., H.O., and W.C. Methodology: L. Zheng, F.C., Z. Li, and W.C. Investigation: T.W., Y.L., E.W., Z. Zhou, L. Zhang, S.T., and Z. Liu. Visualization: X. Li, Y.C., J.X., and L.N. Supervision: L. Zheng, H.O., W.C., and Z. Li. Writing—original draft: T.W., W.C., and Y.L. Writing—review and editing: L. Zheng, F.C., Z. Li, and W.C. **Competing interests:** The authors declare that they have no competing interests. **Data and materials availability:** All data needed to evaluate the conclusions in the paper are present in the paper and/or the Supplementary Materials.

Submitted 13 May 2023
Accepted 1 December 2023
Published 5 January 2024
10.1126/sciadv.adl6799

Rehabilitation exercise–driven symbiotic electrical stimulation system accelerating bone regeneration

Tianlong Wang, Han Ouyang, Yiping Luo, Jiangtao Xue, Engui Wang, Lei Zhang, Zifei Zhou, Zhiqing Liu, Xifan Li, Shuo Tan, Yixing Chen, Liping Nan, Wentao Cao, Zhou Li, Feng Chen, and Longpo Zheng

Sci. Adv. **10** (1), eadi6799. DOI: 10.1126/sciadv.adi6799

View the article online

<https://www.science.org/doi/10.1126/sciadv.adi6799>

Permissions

<https://www.science.org/help/reprints-and-permissions>

Use of this article is subject to the [Terms of service](#)

Science Advances (ISSN 2375-2548) is published by the American Association for the Advancement of Science. 1200 New York Avenue NW, Washington, DC 20005. The title *Science Advances* is a registered trademark of AAAS.

Copyright © 2024 The Authors, some rights reserved; exclusive licensee American Association for the Advancement of Science. No claim to original U.S. Government Works. Distributed under a Creative Commons Attribution NonCommercial License 4.0 (CC BY-NC).